THE SEISMOLOGICAL SOCIETY OF AMERICA
400 Evelyn Ave., Suite 201
Albany, CA 94706-1375
(510) 525-5474; FAX (510) 525-7204
www.seismosoc.org

Bulletin of the Seismological Society of America, Vol. 101, No. 2, pp. 667–687, April 2011, doi: 10.1785/0120100135

Spectral Analysis of K-NET and KiK-net Data in Japan, Part II: On Attenuation Characteristics, Source Spectra, and Site Response of Borehole and Surface Stations

by Adrien Oth, Dino Bindi, Stefano Parolai, and Domenico Di Giacomo*

Abstract In this study we apply a nonparametric spectral inversion scheme to a data set of accelerograms recorded by the K-NET and KiK-net networks in Japan in order to derive attenuation characteristics, source spectra, and site response. For this purpose, we use a total of more than 67,000 *S*-wave records from 2178 earthquakes (M_{JMA} 2.7–8) obtained at 1555 stations at the Earth's surface and more than 29,000 records from 1826 events recorded at 637 borehole stations at depths of 100 to 3000 m. Attenuation characteristics are investigated in five separate regions, showing that crustal Q depicts lower values in central compared to southern Japan, and a significant frequency dependence is observed in every region. The source spectra follow the ω^2 model with higher stress drops for subcrustal earthquakes as compared with crustal ones. While strong amplification effects dominate the site contributions for the surface sensors, those for the borehole sensors are characterized by smaller variability. Nevertheless, consistent with observations from deconvolution of borehole/surface recording pairs, downgoing wave effects are visible in the site contributions for many borehole stations. Finally, the site amplification functions obtained at the surface are compared with surface-to-borehole (S/B) and horizontal-to-vertical (H/V) spectral ratios, showing that the S/B ratios generally provide better estimates of the horizontal amplification than the H/V ratios due to amplification of the vertical component of ground motion.

Introduction

In order to be able to implement appropriate building codes and properly design safety-critical facilities and lifelines in earthquake-prone regions, reliable estimates of the seismic ground shaking that is expected in the future are of utmost importance. These estimates can be formulated either in a deterministic or probabilistic way, yet they always require a profound understanding of the effects that influence observed seismic ground motions. How intense the shaking induced by an earthquake is depends on the source properties of the event, the attenuation of seismic waves on their travel path as well as near-surface amplification effects due to the shallow geological layers beneath the site of interest, and all these effects have to be accounted for in seismic hazard calculations.

The aforementioned contributions are commonly isolated from one another using seismic observations and some spectral modeling or inversion approach, and various authors have dealt with this issue in many regions of the world (e.g., Castro *et al.*, 1990, 1996; Parolai *et al.*, 2000; Moya and Irikura, 2003; Bindi *et al.*, 2004; Salazar *et al.*, 2007; Drouet *et al.*, 2008; Oth *et al.*, 2008, 2009). In order to resolve potential trade-offs, some constraints always need to be applied, and some studies consider specific parametric forms for the source and path components, for instance (e.g., Drouet *et al.*, 2008), while others are based on a nonparametric description (e.g., Castro *et al.*, 1990).

The enormous quantities of high-quality data recorded in the past decade by the seismic networks in Japan deployed following the disastrous 1995 Kobe (Hyogo-ken Nanbu) earthquake (K-NET, KiK-net, Hi-net, and F-net; Okada *et al.*, 2004) provide a unique opportunity to investigate, among others, many important research questions on spectral ground motion characteristics with unprecedented data density, and in recent years, several studies have explored the characteristics of ground motion Fourier amplitude spectra (FAS) in different regions of Japan using different data sets, inversion approaches, and *a priori* assumptions and addressing different focus points (e.g., Jin *et al.*, 2000; Kinoshita and Ohike, 2002; Moya and Irikura, 2003;

*Now at International Seismological Centre, Pipers Lane, Thatcham, RG19 4NS, United Kingdom.

Kawase, 2006; Tsuda *et al.*, 2010). These studies and others all involve more or less restrictive assumptions on the spectral shape (fixing the shape of either source and/or path contributions and, in several cases, simply correcting *a priori* for attenuation with a given Q model), and apart from the work of Kawase (2006), they are all limited to some specific regions in Japan.

In this article, in order to investigate the spectral characteristics of ground motions throughout all of Japan, we apply a nonparametric inversion scheme (Castro *et al.*, 1990) to the largest data set ever used for this purpose (at least to our knowledge), including both surface and borehole recordings. We derive source spectra, attenuation characteristics, and site response functions using only as many constraints as necessary to be able to solve the system of equations, and we do not predefine the functional form of the source spectra or the attenuation operator. We subdivide Japan into five regions and calculate crustal (depth range 0–30 km) and subcrustal (depth > 30 km) nonparametric attenuation functions. We then correct the observations for attenuation and compute source spectra and site amplification throughout the entire country. The appropriateness of typical seismological models for characterizing these nonparametric inversion results is discussed, and in particular, we make use of the insights into the basic features of the data set obtained in Oth *et al.* (2011; hereinafter referred to as the companion paper). Finally, the site response functions are also compared to the typical estimators for site response directly obtainable from the data, that is, horizontal-to-vertical (H/V) and surface-to-borehole (S/B) spectral ratios, and we discuss our results with respect to previous studies as well.

Data Set

This study employs accelerometric recordings provided by the K-NET and KiK-net networks in Japan, and the data set is based on the selection made in the companion paper. The extracted set of seismograms is composed of more than 78,000 surface records from 2201 earthquakes recorded at 1681 K-NET and KiK-net stations as well as about 34,000 borehole records from 1872 earthquakes recorded at 677 KiK-net sites, with borehole depths ranging from 100 m to 3 km. The recorded earthquakes span the magnitude range M_{JMA} 2.7–8. For more information on the K-NET and KiK-net networks and the data processing and selection procedure, we refer the reader to the companion paper.

For the purpose of this study, we use the FAS as calculated in the companion paper, and we only briefly refresh a few important points here. Because of signal-to-noise ratio (SNR) constraints, the analyzed frequency range is limited to 0.5–25 Hz. The FAS were smoothed around 40 frequency points equidistant in a logarithmic scale with the Konno and Ohmachi (1998) windowing function with $b = 40$, and the horizontal components were combined into their root-mean-square average. KiK-net surface and borehole records were corrected for the relative azimuth difference in sensor orientation whenever possible. We only consider weak and not-too-strong motions with peak ground acceleration (PGA) lower than $0.2g$ and only retain events recorded by at least three stations (which was fulfilled for all events in the data set) and stations that recorded at least three events (Fig. 1).

Subdivision of the Data Set: Lateral Attenuation Variability and Event Type Classification

Because we are interested in analyzing the lateral variability in attenuation characteristics, we subdivide Japan into five separate regions (respectively, polygons, Fig. 1) based on the results of an *S*-wave attenuation tomography performed by Pei *et al.* (2009). They found that the volcanic front cutting through the Japanese archipelago represents a clear boundary between east (forearc) and west (backarc) in terms of Q values at a frequency of 1 Hz. For central Japan, we therefore use a rough approximation of the volcanic front as a boundary (polygons 3 and 4, Fig. 1). For southern Japan, due to the setting of the volcanic front and the distribution of earthquakes, we could not use the former as a delimiter between regions. Therefore, we defined polygon 1 such that it encompasses the island of Kyushu, and polygon 2 is composed of Shikoku and southern Honshu. Finally, polygon 5 delimits the island of Hokkaido, where a further subdivision with respect to the volcanic front would

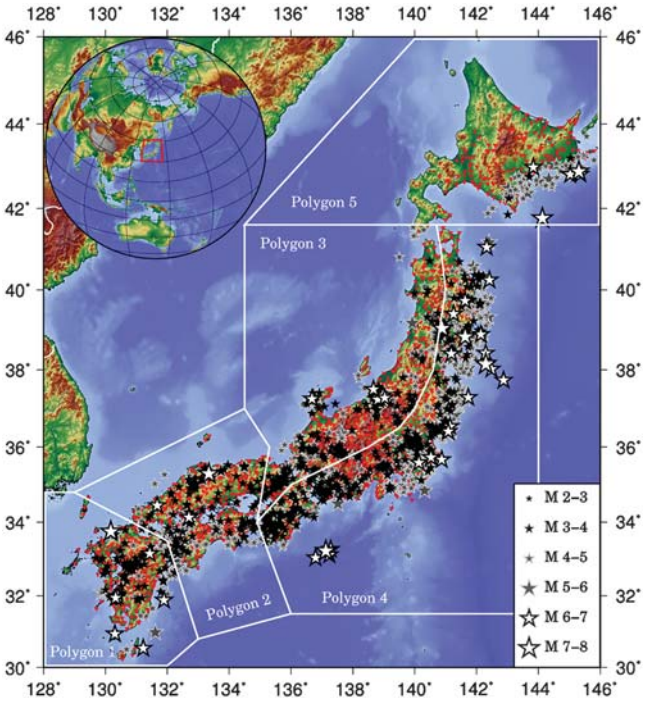

Figure 1. Epicenters of earthquakes (stars) and stations (red inverse triangles, K-NET and KiK-net) considered in this study. For the study of attenuation characteristics, we divided Japan into five polygons, following the attenuation tomography results of Pei *et al.* (2009). Subcrustal earthquakes are primarily linked to the subduction arc in polygons 2, 4, and 5.

not make sense due to the fact that all considered earthquakes are located off the eastern shoreline, leading to a less favorable geometry anyhow. This subdivision of Japan into five polygons represents of course a strong simplification, yet provides a basis for understanding the most relevant lateral variations of seismic attenuation properties and is sensible with respect to the results of Pei *et al.* (2009) as well as similar to the subdivision used by Kawase (2006).

In the following, then, we only consider source-station pairs for which the ray path can be primarily linked to one given polygon. In order to avoid the boundaries of the polygons being too sharp and to couple each polygon to its neighbors for the inversion scheme separating source and site terms later in this article, we chose to include in each polygon's data set all source-station pairs for which 3/4 of the travel path lies within the respective polygon, still maintaining the condition that each event should be recorded by at least three stations and each station should have recorded at least three events. Thus, events and stations slightly beyond the defined boundaries of a given polygon still contribute to the data set for that polygon, and two neighboring polygons share a certain number of events and stations. The only exception is polygon 5 (i.e., Hokkaido) for the borehole data set because the KiK-net station coverage is less dense than the combined K-NET and KiK-net coverage for the surface sensors, and all events in polygon 5 are rather far away from the boundaries with polygons 3 and 4. Therefore, no ray paths coupling polygons 3 and 4 with polygon 5 are included in the borehole data set, and polygon 5 is therefore considered separately also for the separation of source spectra and site amplification functions. These criteria result in the removal of about 11,000 source-station pairs for which the ray paths intersect different polygons. However, because the total data set is extraordinarily voluminous, we do not lose much information by doing so, and the ray coverage is still unrivaled as compared with most other regions of the world.

Depending on their depth, we classified the earthquakes as either crustal (depth $\leq$ 30 km) or subcrustal (depth $>$ 30 km, with maximum earthquake depth in the data set used being ~180 km). This rough classification allows us to study attenuation characteristics of different regions within the Earth's interior (while the propagation of waves generated by crustal earthquakes is also primarily taking place within the crust at local and regional distances, the propagation from earthquake sources in the upper mantle is influenced both by upper-mantle and crustal structure) as well as to get insights into the variability of the source spectra for these two types of events. As shown in figure 2 of Oth *et al.* (2011), the subcrustal events delineate the eastern coastline of Japan and are mostly related to the subduction of the Pacific and Philippine Sea plates.

Hypocentral Distance and M_{JMA} Ranges

The previously mentioned selection criteria finally led to a total data set (i.e., all polygons together) of 67,612 spectra from 2178 earthquakes recorded at 1555 surface sensors and 29,155 spectra from 1826 events recorded at 637 borehole sensors, spanning the magnitude range M_{JMA} 2.7–8. In terms of distance range, we considered hypocentral distances between 5 and 250 km for crustal events and between 30 and 250 km for subcrustal events. Figure 2 shows the distribution of hypocentral distance versus M_{JMA} for the entirety of Japan in both cases. In the case of moderate and larger events, considering 5 km as the lowest hypocentral distance may not be fully compatible with the far-field assumption for the lowest analyzed frequencies. However, because we discarded high PGA records, there are very few data points from moderate and large earthquakes showing a significant amount of energy at low frequencies at these distances remaining in the data set (Fig. 2), and their influence is very limited as compared with the entire data volume.

Table 1 lists the data sets available for analysis of attenuation characteristics (using borehole stations only) within each polygon and for the source/site separation using borehole and surface stations. It should be noted that, due to

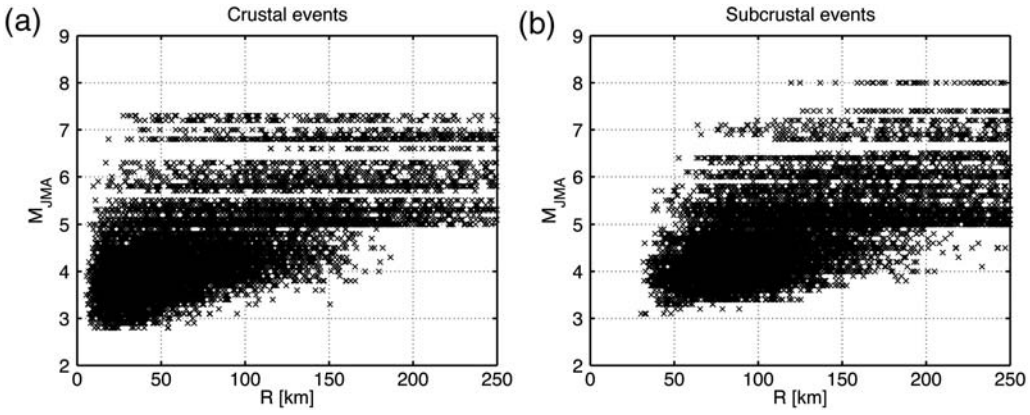

Figure 2. Magnitude (M_{JMA}) versus distance (hypocentral distance R) distribution for (a) crustal and (b) subcrustal events. The distance ranges covered are 5–250 km and 30–250 km for the crustal and subcrustal data sets, respectively. For the GIT inversion considering borehole data only, there are fewer data points because only KiK-net stations can be used, yet still with excellent magnitude-distance coverage.

Table 1
Data Sets Used in the Five Different Polygons* for Investigating Attenuation Characteristics† and Performing the Source/Site Separation with Attenuation-Corrected Data

	Number Records	Number Sites	Number Events	Remarks
Polygon 1 crustal borehole attenuation	1626	78	135	distance range 5–250 km
Polygon 2 crustal borehole attenuation	2132	117	191	distance range 5–250 km
Polygon 3 crustal borehole attenuation	6150	222	453	distance range 5–250 km
Polygon 4 crustal borehole attenuation	3818	210	301	distance range 5–250 km
Polygons 1–4 subcrustal borehole attenuation	14297	422	791	distance range 30–250 km
Polygon 5 subcrustal borehole attenuation	1132	68	55	distance range 75–250 km
Polygons 1–4 borehole source/site	28023	569	1771	attenuation-corrected, inversion for source/site for polygons 1–4 together
Polygon 5 borehole source/site	1132	68	55	attenuation-corrected, subcrustal from polygons 1–4, crustal path from polygon 4
All polygons surface source/site	67612	1555	2178	attenuation-corrected, inversion for source/site for all polygons together

*Shown in Figure 1.
†For subcrustal earthquakes, polygons 1–4 have been considered together while for crustal events, not enough records were available in polygon 5 for studying crustal attenuation in the latter polygon. Because, in the case of the KiK-net borehole data, no ray paths connecting either polygons 3 and 5 or polygons 4 and 5 were in our data set, the source/site separation for the borehole data was performed separately for polygons 1–4 and 5.

the tectonic situation, almost no subcrustal events are located in polygon 3, and very few crustal events took place in polygon 5. For this reason, we could not derive subcrustal and crustal attenuation properties in polygons 3 and 5, respectively. Furthermore, the set of subcrustal earthquakes is dominated by events located in polygon 4, and for Hokkaido (polygon 5), only very few data points are available at hypocentral distances lower than 75 km. Therefore, we analyzed subcrustal attenuation characteristics for polygons 1–4 together and limited the attenuation analysis to distances larger than 75 km in polygon 5 (Table 1).

Effect of Varying Borehole Depths

An important point to consider when using borehole records in such an inversion scheme as presented in the following paragraphs is the fact that the borehole sensors of different stations are located at different depths, ranging from 100 m to 3 km in the case of KiK-net. Because we use the average at all borehole sites as a reference later on, one might argue that it is necessary to correct the borehole records to a common depth by considering the velocity structure within the boreholes. In order to assess the impact of such a correction, we calculated an estimate of the influence on the spectral amplitudes due to the velocity structure below the depth of 100 m for deeper boreholes (200 m or deeper) using the quarter-wavelength approach (e.g., Boore, 2003, with densities computed following equation 3 from Boore and Joyner, 1997), and the results are shown in Figure 3. As can be seen there—even though for a few stations depicting strong velocity contrasts within the deeper part of the profile, the effect may not be negligible (stations with amplification larger than about a factor of 2–3 generally show an interface with significant velocity contrasts in the deeper part of the profile)—on average, the (de-)amplification due to the velocity structure at depths larger than 100 m is insignificant. For that reason, we refrain from correcting all the borehole data to a common depth. However, we do account for borehole depth when calculating hypocentral distances between the sources and downhole sensors, but in this case, borehole depth plays a significant role only for short epicentral distances and deep boreholes.

Generalized Inversion Technique

A common method to isolate frequency-dependent attenuation characteristics, source spectra, and site response

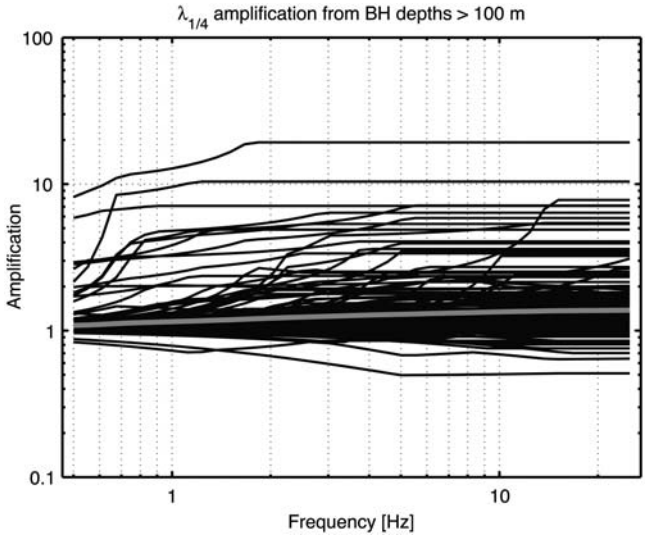

Figure 3. Estimates of amplification for the deeper boreholes (depth ≥ 200 m) resulting from the velocity structure between a depth of 100 m and the bottom of the borehole (i.e., not considering the shallow velocity structure) calculated using the quarter-wavelength approximation. Black lines: individual estimates for 197 boreholes with a final depth of at least 200 m. Thick gray line: average amplification due to the velocity structure at depths > 100 m. See text of paper for more details.

from one another is the generalized inversion technique (GIT) (Andrews, 1986; Castro *et al.*, 1990). In a general way, the FAS of ground motion can be written as

$$U_{ij}(f, M_i, R_{ij}) = S_i(f, M_i) \cdot A(f, R_{ij}) \cdot G_j(f), \quad (1)$$

where $U_{ij}(f, M_i, R_{ij})$ represents the observed spectral amplitude (in our case acceleration) at the jth station resulting from the ith earthquake with magnitude M_i, R_{ij} is the hypocentral distance, $S_i(f, M_i)$ stands for the source spectrum of the ith earthquake, $A(f, R_{ij})$ is the attenuation operator accounting for the path effects, and $G_j(f)$ is the site response function of the jth station. Equation (1) can be linearized by taking the logarithm

$$\log_{10} U_{ij}(f, M_i, R_{ij}) = \log_{10} S_i(f, M_i) + \log_{10} A(f, R_{ij}) + \log_{10} G_j(f). \quad (2)$$

Equation (2) describes a classical linear system of the form $\mathbf{Ax} = \mathbf{b}$, where $\mathbf{b}$ is the data vector containing the logarithmic spectral amplitudes, $\mathbf{x}$ is the vector containing the model parameters, and $\mathbf{A}$ is the system matrix relating them. This system can be solved using appropriate inversion algorithms, yet some constraints always need to be applied, both on the attenuation operator (e.g., Castro *et al.*, 1990) and either on the source or the site response (Andrews, 1986).

The inverse problem described by equation (2) can be handled either with a parametric (e.g., Kawase, 2006; Tsuda *et al.*, 2006, 2010; Salazar *et al.*, 2007; Drouet *et al.*, 2008) or nonparametric (e.g., Castro *et al.*, 1990; Parolai *et al.*, 2000, 2004; Oth *et al.*, 2008, 2009) approach. The latter is very attractive in the sense that if a data set with good distance coverage is available, it allows us to get insights into the potential complexity of attenuation rather than predefining how the operator $A(f, R_{ij})$ should behave. Because the distance coverage is excellent in the case of the K-NET and KiK-net data sets, we prefer to use the nonparametric version of the GIT in this article. The operator $A(f, R_{ij})$ implicitly contains all effects determining the attenuation along the travel path (geometrical spreading, anelastic and scattering attenuation, refracted arrivals, etc.), and based on the idea that these properties vary slowly with distance, $A(f, R_{ij})$ is only constrained to be a smooth function of distance and to take the value $A(f, R_{ij}) = 1$ at some reference distance R_0.

The shape can then be compared *a posteriori* with the expectation from typical seismological models. Morozov (2008) recently proposed to rethink the conventional frequency-dependent attenuation law of the form $Q(f) = Q_0(f/f_0)^N$, such as is used later on in this article as well. We use this type of attenuation model for the sake of comparability with previous studies, but note that from the nonparametric attenuation results obtained in this study, alternative models such the one introduced by Morozov (2008) can be investigated as well. Because we express attenuation in a nonparametric way, the source spectra and site response functions will be independent of any specific model assumptions on the attenuation process, and this independence is a key advantage of the nonparametric technique.

One-Step versus Two-Step Nonparametric Approach

Castro *et al.* (1990) solved equation (2) in two steps: first, the spectral amplitudes are written as

$$\log_{10} U_{ij}(f, M_i, R_{ij}) = \log_{10} \hat{S}_i(f, M_i) + \log_{10} A(f, R_{ij}), \quad (3)$$

with $\hat{S}_i(f, M_i)$ being a scaling factor depending on the size of the ith event. For $A(f, R_{ij})$, the previously mentioned constraints for the nonparametric case are implemented. In the second step, the spectral amplitudes $U_{ij}(f, M_i, R_{ij})$ are corrected for seismic attenuation, and the residual amplitudes $V_{ij}(f, M_i) = U_{ij}(f, M_i, R_{ij})/A(f, R_{ij})$ are separated into source and site contributions:

$$\log_{10} V_{ij}(f, M_i) = \log_{10} S_i(f, M_i) + \log_{10} G_j(f). \quad (4)$$

Here, a common reference condition is to set the site response of a single or a set of rock sites equal to one independent of frequency. For more details on the setup of the matrices for these inversion steps, we refer the reader to Castro *et al.* (1990) or Oth *et al.* (2008).

In the first step of the inversion scheme, given by equation (3), the site effects are necessarily absorbed into $\hat{S}_i(f, M_i)$ and $A(f, R_{ij})$. If the site amplification is relatively similar for all stations (for instance, if all stations are located on rock sites), one can reasonably expect that $\hat{S}_i(f, M_i)$ includes an average amplification contribution for all stations that recorded the ith event and that the deviations of the individual stations from this average are absorbed into the residuals, that is, that the estimate of $A(f, R_{ij})$ should not be systematically biased. However, as already touched upon in the companion paper, K-NET and KiK-net surface stations are subject to severe amplification effects, especially at high frequencies and with strong differences in between one another. In such a case, it is not necessarily clear that the attenuation functions, $A(f, R_{ij})$, obtained by solving equation (3) will be unbiased.

An alternative to the two-step approach consists of simply solving equation (2) directly in one step. To do so, we again constrain $A(f, R_{ij})$ to be a smooth function of distance as well as set $A(f, R_0) = 1$. Furthermore, either one site response function or one source function needs to be fixed as well. The extraordinary attractiveness of this procedure is demonstrated in Figure 4, where we show the results from 100 subsequent one-step inversions, where we impose a randomly varying value to the site constraint in each run. By solving equation (2) directly, the resulting attenuation functions, $A(f, R_{ij})$, are completely independent of the reference condition imposed either on the site response or source spectra (not only on the value, but also on which reference

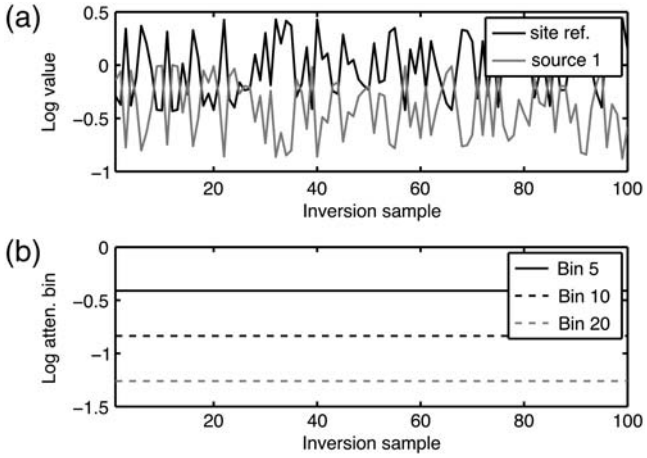

Figure 4. Results of 100 subsequent one-step, nonparametric GIT inversions using the borehole data set in polygon 2, setting the site constraint (average of all stations in this case) to randomly varying values for each inversion sample. The frequency for which these results are shown is 3.36 Hz. (a) Value of the site constraint (black) and value of the first source (gray) resulting from each of the GIT inversions. Any other source could have been chosen, depicting the same anticorrelation. (b) Values of the attenuation function in three distance bins (bin 5, 10, and 20) obtained for each of the 100 GIT inversions.

condition is being used, e.g., whether the average site response or the site response of only one given station is being constrained). Changes in the site constraint result in purely anticorrelated changes in the source contributions. This observation has important consequences, as it means that it is possible to obtain stable results for seismic attenuation even if no appropriate reference site or source is available because the bias introduced by an inappropriate reference condition is not influencing the results for attenuation.

Furthermore, Figure 5 clearly indicates that the estimates of $A(f, R_{ij})$ obtained by solving equation (3) using the surface data are indeed heavily biased, especially at high frequencies where strong amplification effects occur, while this is not the case when solving equation (2) directly in one step. For these reasons, we prefer to follow the one-step nonparametric inversion approach in this study.

Employed Solvers, Constraints, and Specific Remarks

Because we deal with very large matrices, we take advantage of the sparse nature of these and solve the linear systems using the LSQR algorithm (Paige and Saunders, 1982). In order to assess the stability of the inversion results, we perform 100 bootstrap inversions at each frequency point

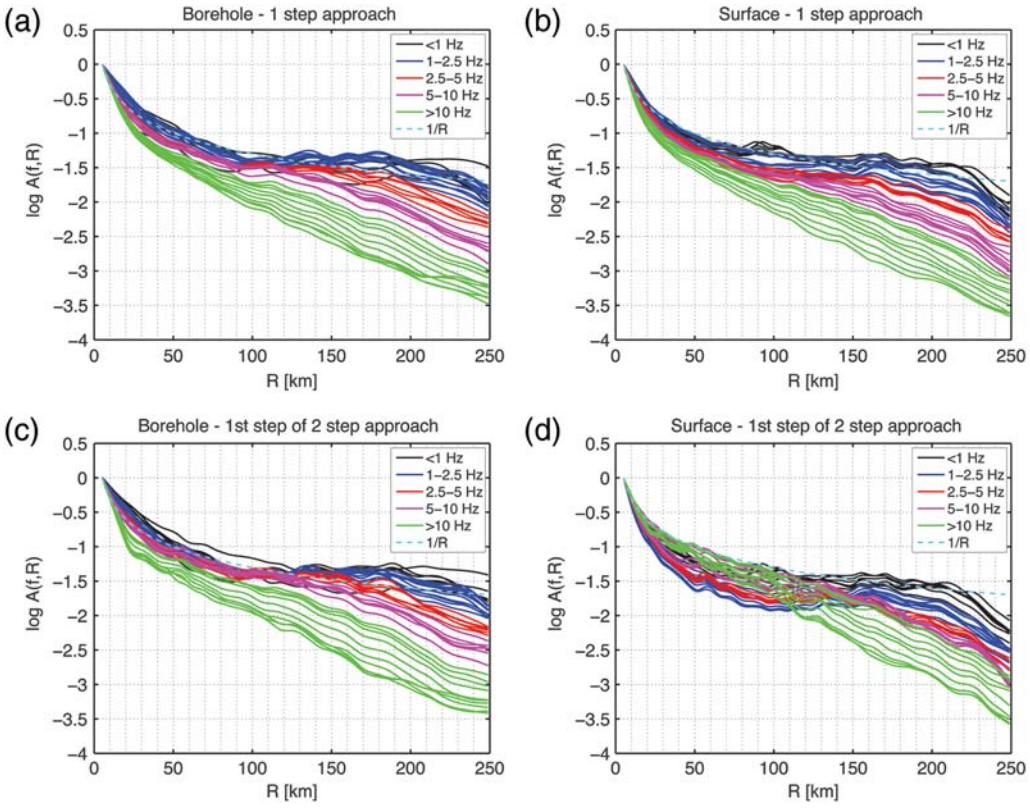

Figure 5. Comparison of nonparametric attenuation functions derived using a one-step GIT approach as defined in equation (2) and using the first step of the two-step GIT approach as described by equation (3). The attenuation functions are shown for all frequencies, color-coded as given in the legend. (a),(c) Results for borehole data in polygon 2 (see also Fig. 1). (b),(d) Results for surface data in polygon 2. For the borehole data, the two approaches lead to comparable results, while for the surface data, the difference is remarkable, especially at high frequencies. Furthermore, using the one-step approach, the attenuation functions derived from borehole and surface data are in good agreement (compare a and b), which is not at all the case for the first step of the two-step approach (compare c and d).

following the procedure detailed in Parolai *et al.* (2000, 2004), and calculate mean as well as standard errors for the model parameters.

Spectral Attenuation with Distance. The nonparametric attenuation functions discussed in this article are determined in each polygon by applying a one-step GIT inversion to borehole recordings only, considering crustal and subcrustal earthquakes in separate inversions.

For polygons 1–4, we solve equation (2) using the borehole records in order to determine nonparametric crustal attenuation functions in each polygon, and the distance range 5–250 km is subdivided into distance bins 2 km wide. As mentioned earlier, for the subcrustal attenuation characteristics, we derived attenuation functions for polygons 1–4 together within a distance range of 30–250 km and for polygon 5 with distance range 75–250 km (Table 1). As a constraint on the site response, we set the average site amplification of all borehole sensors to unity at each frequency point, even though, as mentioned previously, for calculation of attenuation properties only, the choice of this reference does not matter.

Correction for Attenuation Effects. In order to determine site response functions and source spectra relative to the same reference condition for the entirety of Japan, we corrected both borehole and surface ground motion spectra for attenuation using the obtained nonparametric attenuation curves from the one-step GIT inversion for each polygon to a reference distance of 5 km and then separate source and site terms using equation (4) for all of Japan.

In particular, for subcrustal attenuation correction, we first corrected the data to a distance of 30 km and then used the crustal attenuation function in each polygon to correct the spectra back to 5 km reference distance as well. For polygon 5, however, because the data points at hypocentral distances lower than 75 km are sparse, the correction for attenuation is problematic. To nevertheless provide an estimate for source spectra and site response in this region, we used the subcrustal attenuation functions of polygons 1–4 and the crustal attenuation functions of polygon 4 in order to correct the spectra in polygon 5 for attenuation. We are aware that this procedure leads to larger uncertainties for the source and site contributions in polygon 5. However, as we discuss next, the variability observed in attenuation characteristics is not excessively large between the different polygons, and the conclusions regarding source spectra and site response remain unchanged no matter if we include or exclude polygon 5 from the discussion.

Calculation of Source Spectra and Site Response. The ground motion spectra corrected for attenuation are used to determine the source spectra and site response functions by solving equation (4) for all earthquakes and stations throughout Japan, once using the surface (surface sensor site response) and once using the borehole data (borehole sensor site response).

In the case of the borehole data, spectral amplitudes from polygons 1, 2, 3, and 4 are inverted together to isolate the source contribution from the site effects, while the data from polygon 5 are inverted separately due to the missing link between polygons 5 and 1–4 mentioned earlier. We used the average of all borehole stations considered in each of the two inversions (one for polygons 1–4 and one for polygon 5) as a reference condition (i.e., we set the average site response of the borehole stations equal to unity), and because the borehole records should not be strongly affected by amplification effects, we expect to see deviations from the average mainly caused by downgoing waves (see also the companion paper). If we were to constrain the borehole site response to unity at one specific station, the presence of the latter could lead to the shift of the related spectral troughs into the source contributions and, at the same time, corresponding peaks in all inverted site contributions. Because, however, depending on the velocity structure of each borehole, the destructive interference phenomena are located in different frequency ranges and have different amplitudes for each station, a constraint on the average response of the borehole sensors provides a more stable reference with respect to downgoing waves by averaging them out, and spectral troughs visible in the recorded borehole ground motions should show up similarly in their site response function.

For the surface sensors, on the other hand, because these are subjected to very strong amplification effects that are highly variable, the average site response of all stations is not a good reference to use in order to resolve the trade-off between source spectra and site response. Therefore, we needed to find an appropriate reference site. Station YMGH06, located in the border region of polygons 1 and 2, is a good candidate for that purpose because the velocity profile at that station does not show any impedance contrasts at shallow depth (fig. 8 of the companion paper), with average shear wave velocity of the upper 30 m, $v_{S30} = 2.1$ km/s, corresponding to a hard rock site (National Earthquake Hazards Reduction Program [NEHRP] class A, International Code Council, 2006). Furthermore, the S/B and H/V ratios are flat and close to unity (see Figs. 14 and 15).

Attenuation Characteristics

As listed in Table 1, crustal attenuation functions have been calculated for the individual polygons 1, 2, 3, and 4, while for subcrustal propagation, polygons 1–4 were grouped together, and for polygon 5, only subcrustal propagation paths could be considered. The GIT reference distance was $R_0 = 5$ km in the crustal and $R_0 = 30$ km in the subcrustal case ($R_0 = 75$ km for polygon 5). Figure 6 shows the crustal attenuation functions obtained in polygon 4 for two different frequencies together with the spectral amplitudes corrected for source and site terms as derived from the one-step GIT inversion. In general, the obtained attenuation

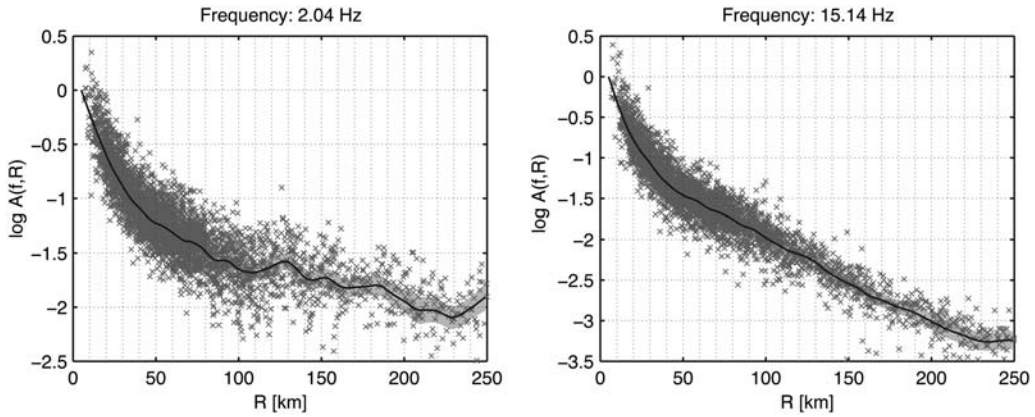

Figure 6. Attenuation function, $\log A(f, R)$ with R being hypocentral distance, for crustal earthquakes in polygon 4 at two given frequencies. The standard deviation calculated by bootstrap resampling is indicated as a gray-shaded area around the mean (solid black line). Note that $\log A(f, R_0) = 0$, with reference distance $R_0 = 5$ km. The dark gray crosses represent the recorded spectral amplitudes, corrected for source and site contributions as derived from the GIT inversion described in equation (2).

functions describe the distance decay of the corrected spectral amplitudes very well, with somewhat higher scatter at low frequencies. This higher scatter may reflect both lower SNRs (even though still larger than 3) and the fact that at lower frequencies, the spectral amplitudes may still show a significant deterministic component of the radiation pattern (e.g., Takenaka *et al.*, 2003, who found that double-couple radiation patterns were recognizable up to a frequency of about 2 Hz), which is not accounted for in the spectral model.

In Figure 7, the crustal nonparametric attenuation functions for polygon 4 (left panel) and the subcrustal ones for the combined polygons 1–4 (right panel) are depicted for all 40 frequency points between 0.5 and 25 Hz. In the case of crustal attenuation, the curves generally show a rapid decay within the first 40–50 km and slowly start flattening beyond that distance. At low frequencies ($< \sim$2 Hz), they show a relatively distinct kink at about 90 km distance, from whereon they are almost entirely flat. On the other hand, the subcrustal attenuation functions show much simpler characteristics, with similar amplitude decay along the entire distance range. These observations suggest that at large distances, the crustal attenuation curves might be influenced by critically reflected or refracted waves from the Moho, an observation also made by Bindi *et al.* (2006) in northwestern Turkey, whereas the *S*-wave windows selected from subcrustal events are always related to direct wave arrivals. In terms of attenuation of different frequency components, as expected, the high-frequency attenuation curves decay more rapidly than the low frequency ones, and while the previously mentioned kink in crustal attenuation at a distance of about 90 km is very clear at the lowest frequencies, its strength decreases rapidly with increasing frequency. This is in agreement with the idea that the lowest frequencies are subjected to lower attenuation, and for the high-frequency components also, the reflections from the Moho will have been significantly affected by attenuation effects at the moment they return to the observation point at the Earth's surface.

In order to express attenuation in terms of a nondimensional quality factor, $Q(f)$, we fit the following equation to the nonparametric curves:

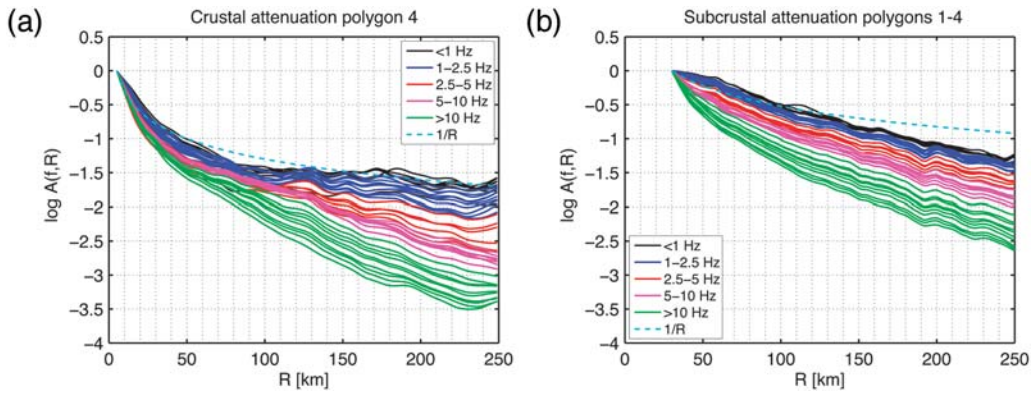

Figure 7. Attenuation functions, $\log A(f, R)$ with R being hypocentral distance, for all frequencies for (a) crustal events in polygon 4 and (b) subcrustal events in polygons 1–4. Different frequency ranges are color-coded as detailed in the legend of the plot. For comparison, a $1/R$ amplitude decay is indicated as a dashed cyan line.

$$A(f,R) = \frac{C}{R^n}\exp\left[-\frac{\pi f(R-C)}{Q(f)v_S}\right], \quad (5)$$

where v_S is the shear-wave velocity, C is the reference distance set for the fit, and n is the geometrical spreading exponent. Three important points should be noted at this stage: First, because our nonparametric functions implicitly include all effects leading to attenuation of seismic wave energy, the quality factors obtained by fitting equation (5) to the attenuation curves include both anelastic and scattering attenuation. Second, since the simple functional form of equation (5) cannot account for the complexities observed in crustal attenuation at larger distances, we only use the distance range 10–50 km for the fits in the case of crustal propagation, while we use the distance range 50–150 km for the subcrustal attenuation functions (and, because for polygon 5 the data set used to derive attenuation characteristics starts only at 75 km distance, we use the distance range 75–150 km in that case). Third, there is a trade-off in the determination of n and $Q(f)$, and it is a difficult issue to derive reliable estimates for them together. For this reason, in order to obtain stable estimates of $Q(f)$, and because we consider the parts of the attenuation curves that are likely to be dominated by direct-wave propagation, we set $n = 1$ and restrict our discussion on the calculation of $Q(f)$ (which is performed through least-squares fitting in logarithm). Finally, from the derived $Q(f)$ values, the parameters Q_0 and N, describing the frequency-dependence as $Q(f) = Q_0 f^N$, can be derived through a least-squares fit as well. Of course, with this fitting procedure, we impose a strong assumption on geometrical spreading, and the obtained $Q(f)$ results are only valid under this assumption, that is, they represent one possible interpretation of the nonparametric attenuation functions. As mentioned earlier, we use this type of model in order to allow for a comparison of our results with previous studies, but the nonparametric attenuation curves could also be interpreted using alternative models (e.g., Morozov, 2008).

Figure 8 shows the $Q(f)$ results obtained for the different polygons, respectively, crustal and subcrustal propagation paths as well as the models $Q(f) = Q_0 f^N$ (solid lines), the results for Q_0 and N also being listed in Table 2. As a general rule, the latter parameterization describes the $Q(f)$ values very well. Crustal attenuation is strongest in polygons 3 and 4, with almost no difference between the forearc (polygon 4) and backarc (polygon 3) region relative to the volcanic front, which is, at first glance, in contradiction to the results of Pei *et al.* (2009). However, even with our subdivision into five polygons, we are of course still averaging attenuation characteristics over relatively large areas, and also, polygon 4 includes regions with stronger attenuation, for instance, off the northeastern shoreline of Honshu close to the Japan Trench (Pei *et al.*, 2009). As a general observation, $Q(f)$ is in all cases strongly frequency dependent, with N ranging between 0.6 and 0.9. Polygons 1 and 2 show larger $Q(f)$ values than polygons 3 and 4 in terms of crustal characteristics, but with slightly weaker frequency dependence.

The $Q(f)$ results derived from the subcrustal travel paths depict only slightly larger values than the ones obtained in most polygons for the crustal case, and there is only little difference between the frequency dependence and fitted Q_0 values in polygons 1–4 and 5. The former observation emphasizes that, obviously, the subcrustal attenuation functions also seem to map mostly the more strongly attenuating crustal structure that the waves pass on the their way to the stations, with the main difference being the fact that the wave field consists of direct waves over the entire distance range.

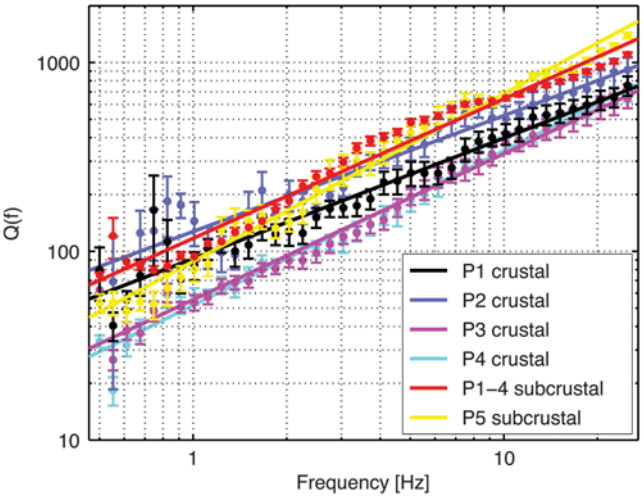

Figure 8. $Q(f)$ models derived from analysis of the nonparametric attenuation functions from GIT inversion for the polygons shown in Figure 1. The parameters Q_0 and N as well as the considered distance ranges are specified in Table 2. Note that all models show a significant frequency dependence, with N ranging between 0.6 and 0.9.

Table 2

Q Models Derived for the Different Polygons from Data Sets Considering only Crustal and Subcrustal Events

	Q_0	N
Polygon 1 crustal	91 ± 8	0.64 ± 0.05
Polygon 2 crustal	127 ± 13	0.61 ± 0.06
Polygon 3 crustal	55 ± 4	0.77 ± 0.04
Polygon 4 crustal	51 ± 3	0.82 ± 0.04
Polygons 1–4 subcrustal	117 ± 9	0.74 ± 0.04
Polygon 5 subcrustal	88 ± 6	0.89 ± 0.04

For crustal attenuation characteristics, the nonparametric attenuation functions in the distance range 10–50 km were used, whereas for subcrustal attenuation, the distance ranges 30–150 km and 75–150 km were used for polygons 1–4 and 5, respectively. The models listed in this table are graphically displayed in Figure 8.

Overall, the $Q(f)$ values between the different polygons all range within a factor of about 2 from one another, and this outcome also suggests that, because the correction for attenuation using the attenuation functions derived in polygon 5 is not easily feasible due to the less favorable geometry and distance coverage, it is probably a fair approximation to use attenuation functions derived in polygons 1–4 for subcrustal attenuation and polygon 4 for crustal attenuation to correct the FAS from the subcrustal events in polygon 5 before separation of source and site terms.

Source Spectra

Having determined and discussed the main features of attenuation properties in the previous section, we corrected the ground motion FAS for attenuation and separated them into their source and site contributions following equation (4) for the entire Japanese data set. Because of the limited space available and the multitude of results to be presented, we only briefly address the source spectral shape in this section, and a detailed discussion on source parameters (scaling characteristics, scaled energy, and the relation between M_{JMA} and M_w) of the Japanese earthquakes is provided in a separate article (Oth *et al.*, 2010).

Figure 9 shows several examples of source spectra at 5 km reference distance derived from the borehole (solid gray lines, with standard deviation from 100 bootstrap samples as black shading) and surface (solid black lines, with standard deviation as gray shading). As can be seen from the standard deviations, the source spectra estimates are generally very stable. Another striking observation is the fact that the source spectra derived from borehole and surface data show a good agreement with one another at frequencies lower than about 6 Hz. At higher frequencies however, the source spectra obtained from the surface data inversion decay rapidly while their borehole counterparts show almost no decay at all.

This discrepancy at high frequencies is linked to the fact that we did not include a high-frequency κ decay term of the form $\exp(-\pi\kappa f)$ (Anderson and Hough, 1984; Boore, 2003) either in the site constraint for the borehole (average site response equal unity) or for the surface data (station YMGH06 equal unity). For that reason, we expect to see the high-frequency decay of the reference that was not accounted for in the inverted source contributions. This high-frequency

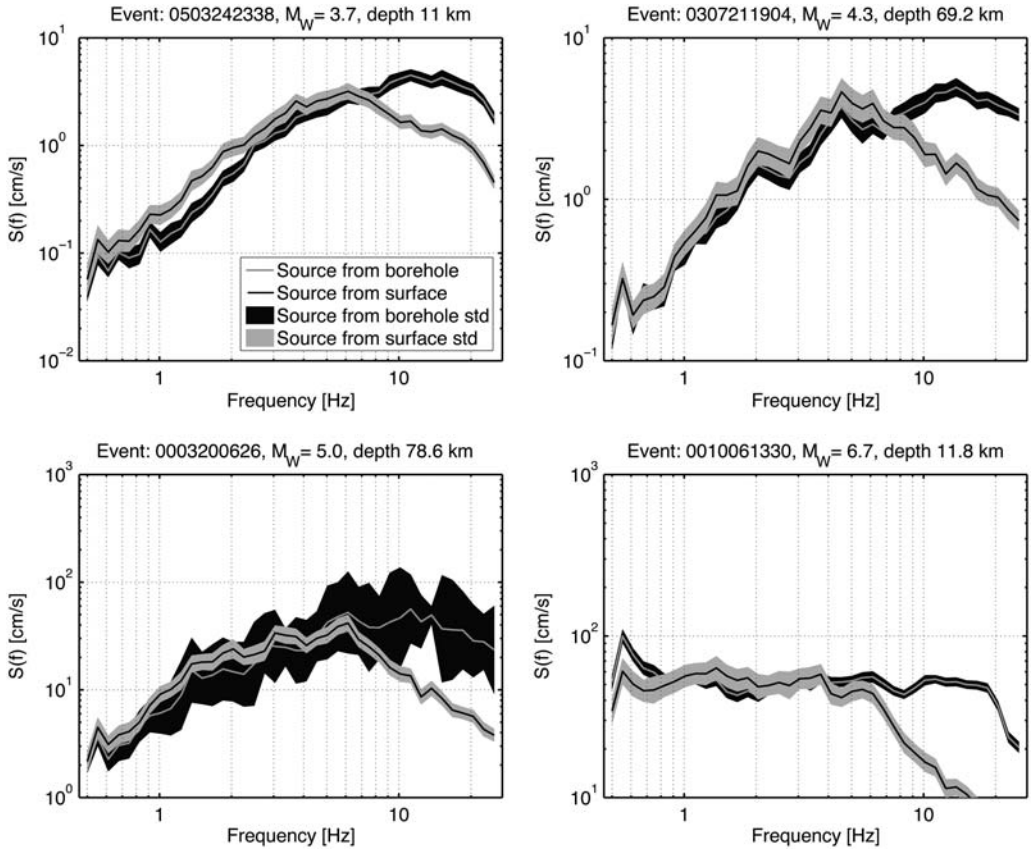

Figure 9. Examples of acceleration source spectra derived from GIT inversion of KiK-net borehole (gray line, average; black area, standard deviation of bootstrap samples) and surface (black line, average; gray shaded area, standard deviation of bootstrap samples) data for four events with moment magnitudes M_w 3.7, 4.3, 5.0, and 6.7. The last of these events is the 2000 Tottori earthquake. Note the strong decay of the sources from the surface data at frequencies higher than about 6 Hz. At lower frequencies, there is a good agreement between the two estimates.

decay of ground motion spectra is thought to be linked to attenuation within the near-surface weathered layers (Anderson and Hough, 1984), but source (Papageorgiou and Aki, 1983) and propagation effects (Hanks, 1982) have also been invoked as explanations.

We systematically evaluate the κ decay remaining in the source spectra (both from borehole and surface data) by fitting the following relation to the high-frequency part:

$$\log_{10} S_i(f > f_E) = S_{0,i} - \log_{10} e \cdot \pi \kappa_i f, \qquad (6)$$

with f_E being the lower frequency bound considered (Anderson and Hough, 1984). As Parolai and Bindi (2004) noted, in order to obtain reliable κ estimates, the measurements should be performed well beyond the corner frequency of the events. In view of the magnitude range of the events considered in this study, we tested both using $f_E = 10$ Hz and $f_E = 15$ Hz without significant differences in the overall results (here we show the results obtained with $f_E = 10$ Hz), but note that in principle, f_E would have to be chosen appropriately for each individual spectrum.

The distribution of κ values for crustal earthquakes is shown in Figure 10 for the borehole (left) and surface (right) case. κ is approximately normally distributed with mean values 0.015 and 0.029 s, respectively. The results obtained for subcrustal events are very close to these values as well. The normal distribution reflects the fact that the κ term remaining in the source spectra is indeed simply related to a missing κ term in the reference site condition shifted into the sources (and thus, on average, the source spectra should also all be subjected to the same reference κ decay). As Oth *et al.* (2009) discussed, differences in high-frequency decay due to variability in near-surface attenuation between different sites should, however, be accounted for in the calculated site amplification functions.

The obtained κ values from the borehole data are very small, whereas those from the surface data are in the range of values typically expected for hard rock sites at the Earth's surface (between 0.02 and 0.04 s; see, e.g., Hartzell *et al.*, 1996; Boore, 2003), thus showing that the borehole records are undergoing comparatively little remaining high-frequency diminution after attenuation along the travel path has been accounted for. Furthermore, the difference in high-frequency decay between the borehole and surface data also indicates that the stronger κ decays observed at surface stations are indeed primarily linked to near-surface attenuation effects. Whether the remaining decay at the borehole sites is, however, related to an effect at borehole depth or rather linked to the source process needs to be investigated in future research (a part of this remaining high-frequency diminution may also result from the slight decay in the instruments' transfer function amplitude characteristics for $f > \sim$15 Hz; see also the companion paper).

The link between the source spectra as derived from borehole and surface data can also be expressed by simply considering the ratios between the two, and the obtained function of frequency shown in Figure 11, F_{corr}, is well constrained (thus showing that there is a strong systematic link throughout the entire data set) and could, in principle, be used to shift the reference to borehole depth when discussing the site amplification functions of the surface sensors in the following section (which, as calculated in the inversion, are relative to the site response at YMGH06 and are assumed equal to one). These reference-shifted site response functions would then include the effect of high-frequency, near-surface attenuation.

We assessed the κ-corrected source spectra as derived from the borehole data set in terms of the ω^2 model (Aki, 1967; Brune, 1970, 1971), and calculated corner frequencies, seismic moments, stress drop, and radiated energy of the earthquakes, and the results of this analysis are discussed in detail in a dedicated article (Oth *et al.*, 2010). Summarizing the findings presented there, the source spectra can be well explained using the ω^2-model (see examples in Fig. 12), and both crustal and subcrustal earthquakes show self-similar scaling characteristics over the entire magnitude

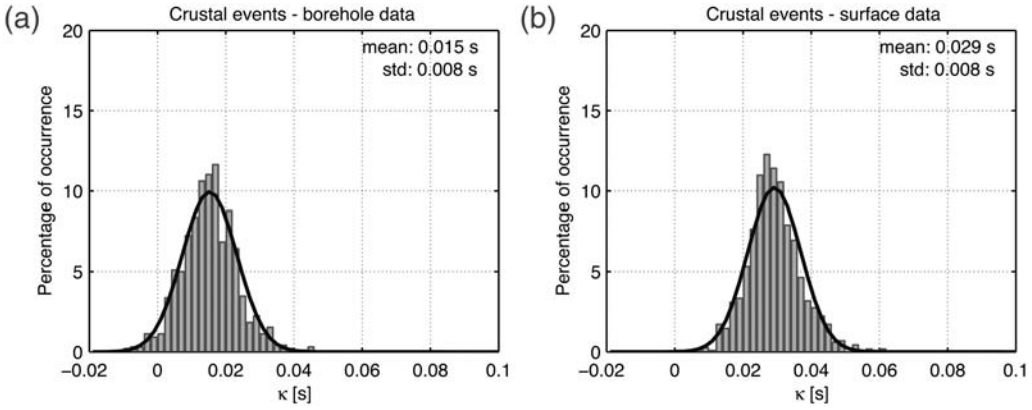

Figure 10. κ distributions resulting from analysis of source spectra obtained from GIT inversion of (a) borehole and (b) surface data. In both cases, κ values are approximately normally distributed, with a larger average for the surface data, reflecting near-surface diminution of high-frequencies at the reference site YMGH06 as described by Anderson and Hough (1984).

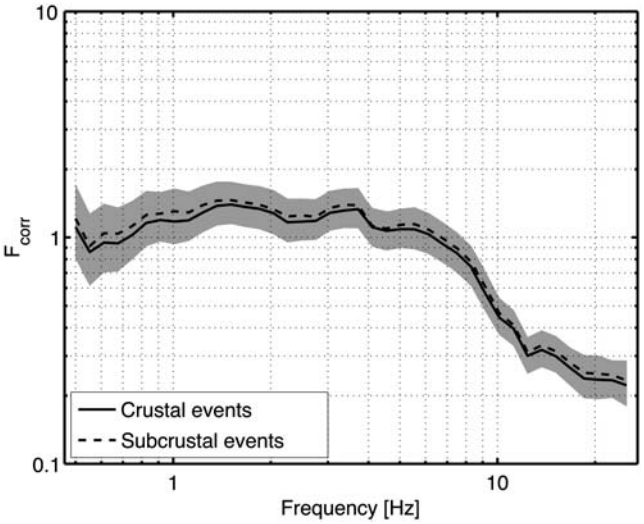

Figure 11. Average correction factor F_{corr}, calculated as the ratio between the source spectra derived from GIT inversion of surface and borehole data. The average of F_{corr} is well constrained with small standard deviation (gray shaded area).

range, with stress drops higher by one order of magnitude for subcrustal events (on the order of 10 MPa) as compared with crustal events (on the order of 1 MPa).

Site Response: Borehole and Surface Stations

As already mentioned, the attenuation-corrected FAS were separated into their source and site contributions following equation (4) for the borehole and surface data sets separately, considering once the horizontal (H) and once the vertical component (Z) data for the latter. This way, we obtained site response functions for the H and Z surface (constraining site amplification at station YMGH06 to be equal to unity, irrespective of frequency) as well as H borehole data (constraining the average of the site response at all borehole stations to be equal to unity). Through additional analysis of the Z component of the surface recordings, we are able to assess the effect of Z component amplification and its impact on the H/V ratios. In this case, a reference site for which both the amplification of the H and Z component can be reasonably assumed to be negligible is required, and as mentioned earlier, station YMGH06 is a good candidate for that purpose.

Figure 13 shows the site response functions obtained for the H component at surface and borehole depth at six KiK-net stations that provide a good sample of the typically observed effects and whose locations and seismic velocity profiles are provided in figures 5 and 8 of Oth *et al.*

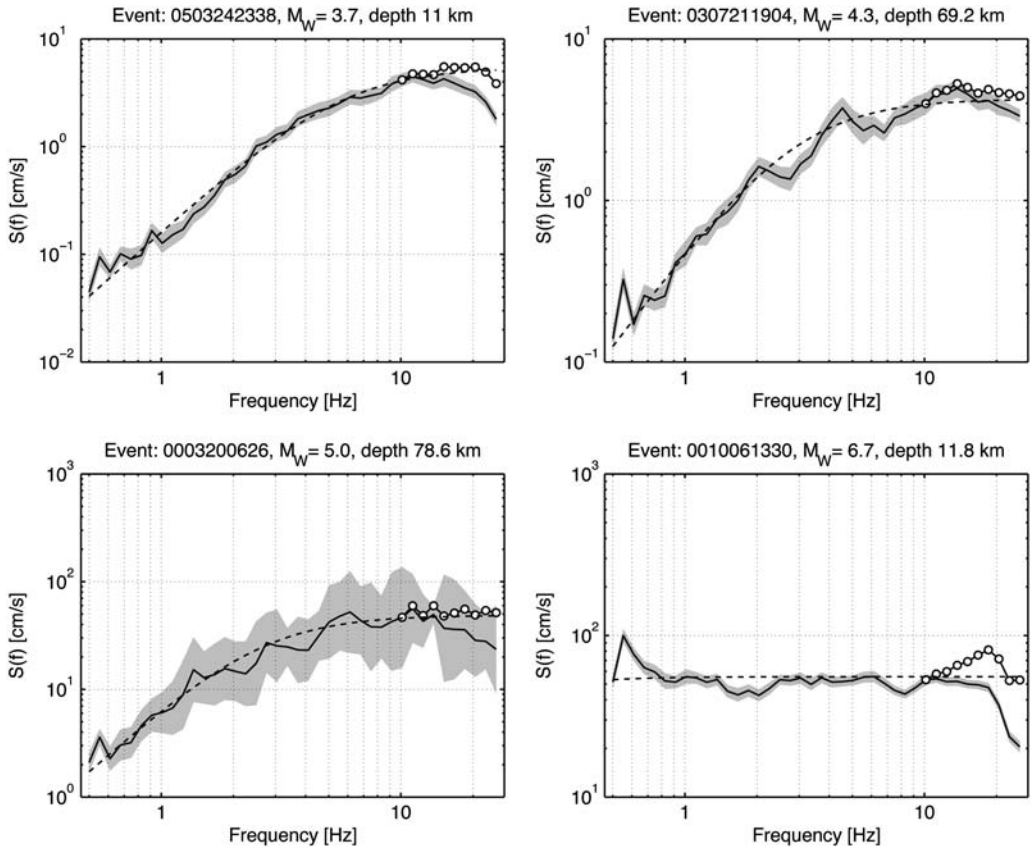

Figure 12. Same source spectra as derived from the borehole data set as shown in Figure 9, this time in conjunction with the ω^2 fitted theoretical source spectra. The results from the GIT are shown as solid black lines (source spectra at reference distance $R_0 = 5$ km), with the gray shaded area marking the standard deviation from bootstrap analysis. These source spectra have been corrected for κ decay for frequencies larger than 10 Hz (indicated with white circles) before fitting with an ω^2 source model (dashed line).

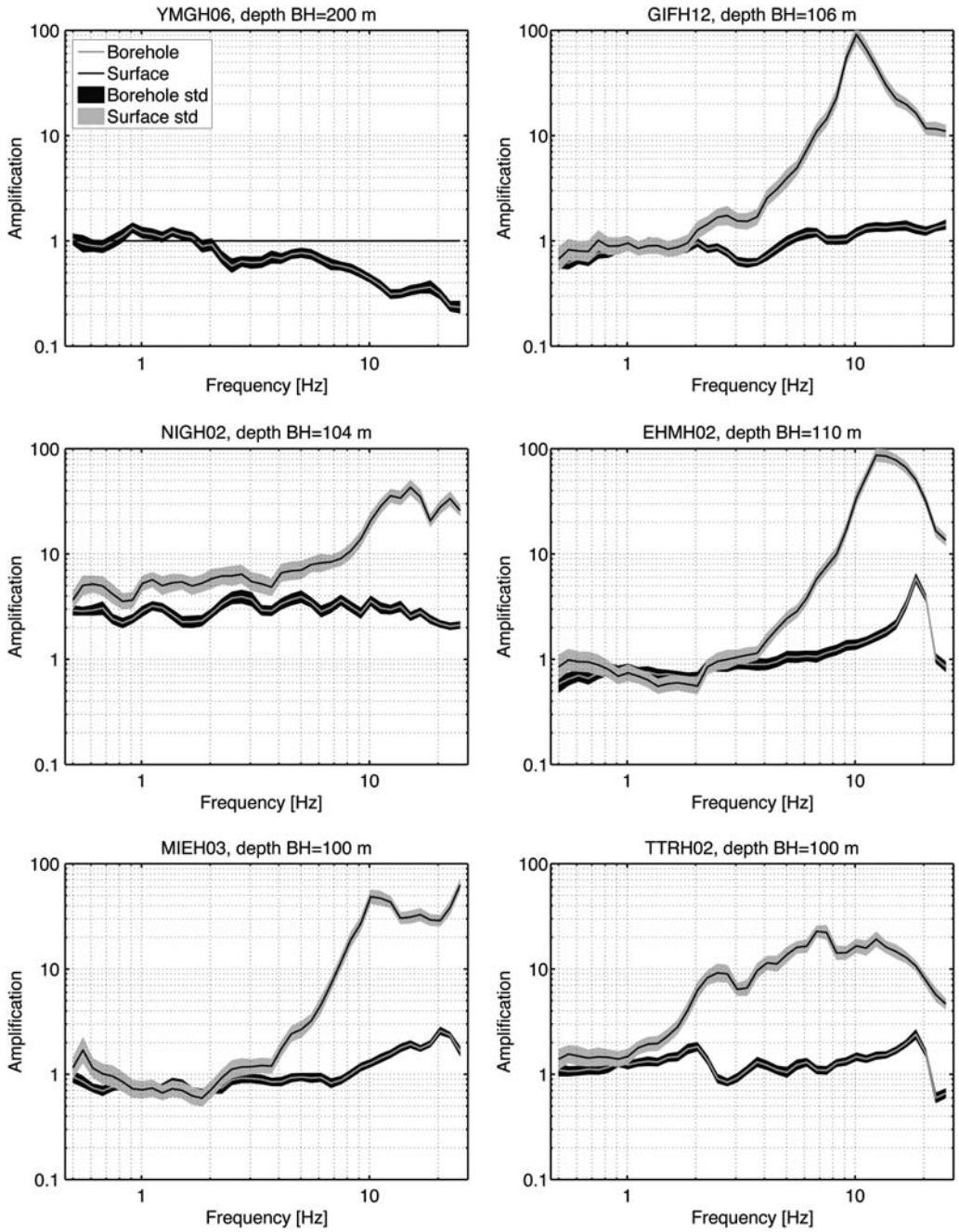

Figure 13. Site amplification functions obtained from GIT H inversion at six KiK-net stations. Shown are both the results for the borehole (solid gray line, bootstrap mean; black area, bootstrap standard deviation) and surface (solid black line, bootstrap mean; gray shaded area, bootstrap standard deviation) sensors. Note that for the surface data inversion, the amplification at station YMGH06 was supposed to be equal to one over the entire frequency range, whereas for the borehole data inversion, the average amplification at all sensors was supposed to be equal to one.

(2011). Because station YMGH06 is the reference station for the surface data, the inverted site response is of course equal to unity in that case. As expected from the first overview on the spectral properties given in the companion paper, strong amplification effects are visible in the surface results, with factors up to 100 relative to the reference, and many sites show peak resonance frequencies around 10 Hz or higher. These sometimes extremely large amplifications at high frequencies are difficult to explain with simple resonance caused by near-surface impedance contrasts alone, and other effects may play an important role as well. Such effects include the influence of the topography, conversion of body to surface-wave energy, but soil-structure interactions with the observation sheds may also be a candidate leading to severe amplification of the surface records. For instance, the peak frequency of the amplification function at about 7–8 Hz at station TTRH02 is most

likely related to vibrations of the observation house (Yoshimura *et al.*, 2003; Maeda, 2004). As Maeda (2004) also noted, the velocity in the near-surface layers at station TTRH02 is likely to be lower than the value obtained from *PS* logging, and local high-frequency surface waves potentially generated in a thin near-surface soft layer unresolved in the *PS*-logging data may explain these very high amplifications (at least partially) at other stations as well.

For the borehole sensors, on the other hand, the variability in the site response functions is, of course, much lower due to missing amplification effects, most of them ranging quite close around the average, which was constrained to unity. However, spectral troughs due to destructive interference effects caused by downgoing wave propagation can be well identified and are in excellent agreement with the features observed directly from the spectra of borehole

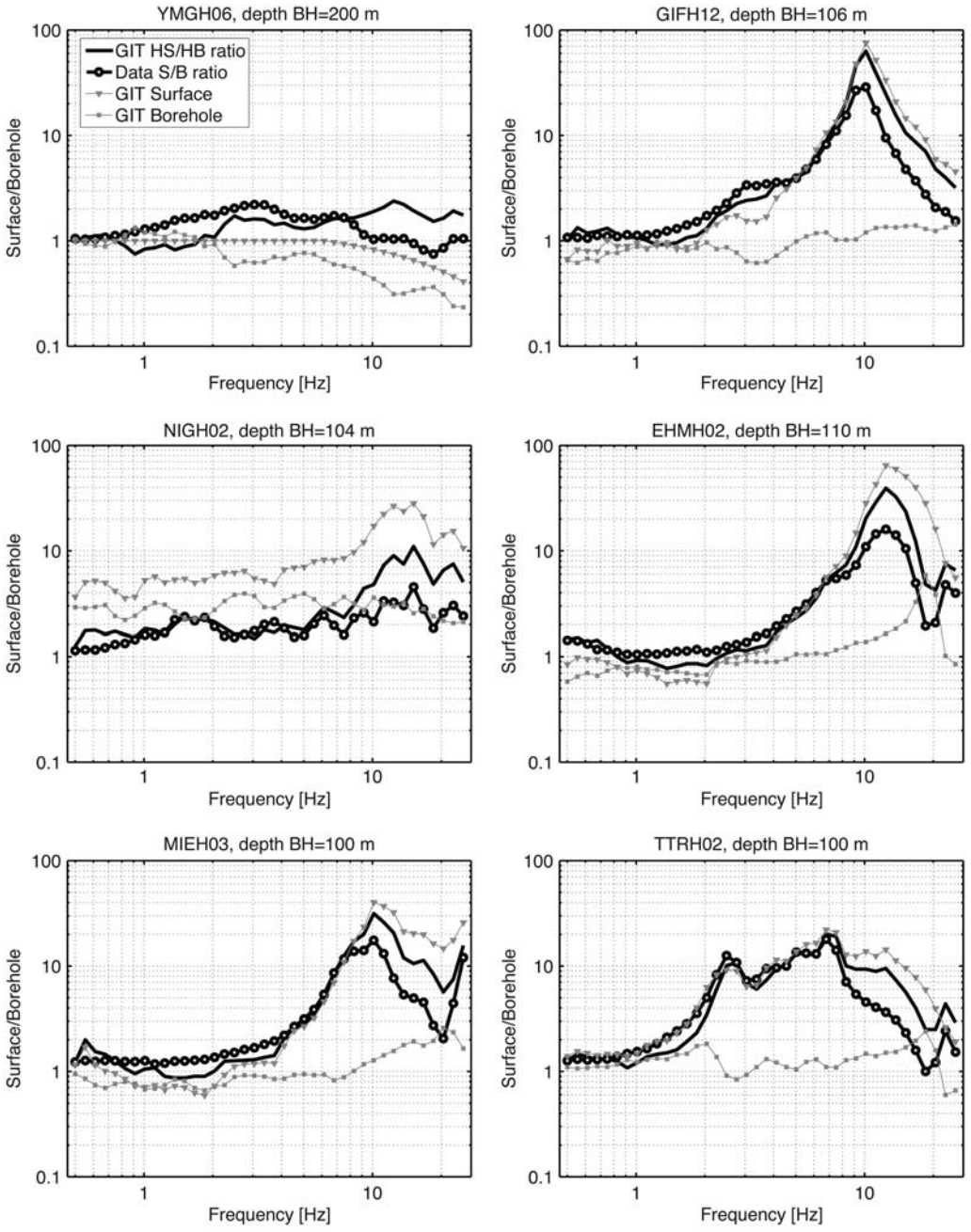

Figure 14. Comparison of S/B ratios directly calculated from the FAS of the recordings (black line with circles) and GIT HS/HB ratios (i.e., H component amplification function at surface divided by the one at borehole depth, solid black line) for the six KiK-net stations already discussed in Figure 13. Additionally, the GIT amplification functions at surface and borehole depths are also indicated as gray lines with inverse triangles and squares, respectively. Note that in this plot, the surface amplification functions have been corrected by the average differential κ decay between surface and borehole source spectra (Fig. 10 and text).

ground motions (e.g., stations GIFH12 and TTRH02 in the frequency ranges 2–7 Hz and 2–4 Hz, respectively, compare with fig. 4 of the companion paper). Moreover, the source spectra derived from the borehole records (Fig. 12) as well as the relation between source spectra derived from borehole and surface data (Fig. 11) do not show any systematic contamination in the form of spectral troughs, which is another good indication that downgoing wave effects are not shifted into the source contributions. Thus, the GIT inversion approach proves to be a powerful tool for understanding the impact of downgoing wave propagation on the ground motion spectra of borehole records.

In Figures 14 and 15, we compare the results from the GIT inversion with the S/B and H/V ratios directly calculated from the observed spectra, respectively. For this purpose, we calculate the ratios of site amplification functions inverted using surface and borehole H component recordings, GIT HS/HB, as well as those calculated for H and Z components

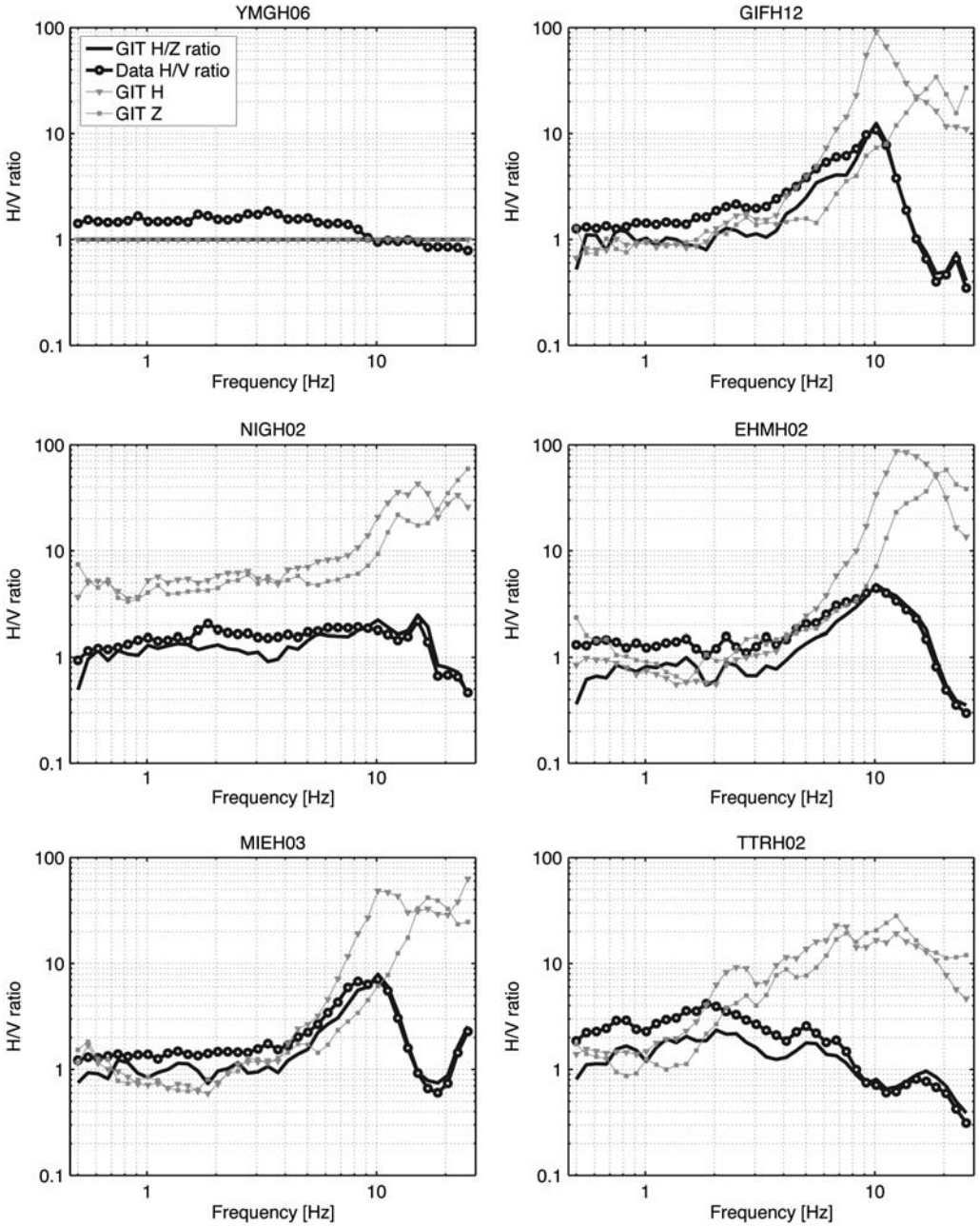

Figure 15. Comparison of H/V ratios directly calculated from the FAS of the recordings (black line with circles) and GIT H/Z ratios (i.e., amplification function of H component divided by amplification function of Z component) for the six KiK-net stations already discussed in Figures 13 and 14. Additionally, the amplification functions of the H and Z components are also indicated as gray lines with inverse triangles and squares, respectively.

of the surface records, GIT H/Z. In order to better understand how the structure of the GIT HS/HB and GIT H/Z ratios is generated, we also show the individual amplification functions in each case. As we discussed in the framework of the seismic source results, when comparing the GIT HS/HB with S/B ratios obtained directly from the data, we need to consider the fact that the reference conditions set for the surface and borehole GIT inversions are different with respect to high-frequency decay shifted into the source results. While the reference conditions are similar in the sense that both the average borehole site response and the one on the rock site YMGH06 should be free of severe amplification effects, the surface reference condition does not account for additional high-frequency decay with respect to the borehole average induced by near-surface attenuation of high-frequency ground motions due to the presence of weathered layers close to the surface. This leads, on average, to the stronger high-frequency decay of the source spectra computed using the surface data set (it can be seen from Fig. 10 that the average difference in estimated κ values is approximately $\kappa_{\mathrm{diff}} = 0.015$ s). Figures 9 and 11 show that the decay starts at lower frequencies (around 6 Hz) in the surface records as compared with the borehole ones as well. Therefore, when calculating the GIT HS/HB ratios, we applied the filter $\exp(-\pi\kappa_{\mathrm{diff}} f)$ to the surface amplification functions for frequencies larger than 6 Hz (see station YMGH06 in Fig. 11). This way, we ensure that the references set for borehole and surface site responses when comparing GIT HS/HB and S/B ratios are approximately equal. Note that we could also have used the empirical correction function $F_{\mathrm{corr}}(f)$ shown in Figure 11 to correct the surface amplification functions to the same reference as the borehole ones. However, for the purpose of our discussion, we prefer to perform and discuss this correction in a way that can be easily associated with common parameters in spectral ground motion models (κ in this case) instead of simply using the empirical correction without associating a clear meaning with it. This problem does not affect the comparison of GIT H/Z ratios and H/V ratios because, for the surface H and Z GIT inversions, the reference condition is identical.

In general, the fits between GIT HS/HB and S/B ratios as well as between GIT H/Z and H/V ratios are good to excellent, and the prominent features in the observed S/B and H/V ratios can be well reproduced. The GIT HS/HB ratios are usually a little bit larger than the S/B ratios at high frequencies, which may be linked to a remaining slight difference in reference conditions even after the correction with κ_{diff}. The small deviations between GIT H/Z and H/V ratios at frequencies lower than 10 Hz are related to the fact that, due to the reference conditions, the GIT H/Z ratio at the reference site YMGH06 is exactly equal to unity while the observed H/V ratio is slightly larger.

Figure 15 shows that the Z component of ground motion at the Earth's surface can be subjected to considerable amplification effects as well. Interestingly, the main peaks of the latter are usually at higher frequencies than for the H component, and in quite a few cases, the shift in frequency is relatively close to a factor of $\sqrt{3}$ (e.g., GIFH12 or EHMH02). A possible explanation for this behavior is that *S-P* conversions generated at strong impedance contrasts lead to *P*-wave resonance effects on the vertical component and cause the latter to be amplified as well (Parolai and Richwalski, 2004). Stations where this effect is particularly remarkable usually show extraordinarily strong *P*-wave velocity contrasts (compare with velocity profiles in fig. 8 of the companion paper).

The site responses obtained with different techniques for a large set of stations can also be compared in terms of some general parameters characterizing them, such as peak frequency and peak amplitude. We automatically picked these parameters for the surface site response functions using the following procedure (which is a slightly modified version of the approach used by Tsuda *et al.*, 2010): For a given site amplification function at a given station (GIT H corrected with κ_{diff}, S/B, or H/V), we picked all local maxima, the two local minima on the left and right of the global maximum, and the global minimum. If the amplitudes of the two local minima are both less than half of the amplitude of the global maximum, the global maximum is at least a factor of 5 larger than the global minimum, and all local maxima have amplitudes less than three-fourths of the global maximum, then we retain the frequency and amplitude values of the global maximum. Otherwise, no peak frequency and amplitude can be chosen for this site response estimator at the given observation site.

Figure 16 shows the comparison of peak frequency (top panels, we have smoothed the spectra around 40 frequency points equidistant in log scale, two points adjacent to each other either on the x or y axis have always identical distances) and peak amplitude (bottom panels) for H/V versus GIT H, S/B versus GIT H and S/B versus H/V. Parolai and Richwalski (2004) showed that the H/V ratio is often able to correctly identify the fundamental resonance frequency; however, it tends to fail in amplitude due to amplification of the Z component caused by *S-P* conversions at the base of the soft layers. This is precisely what we also observe in Figure 16, where the H/V peak frequency is usually lower than or equal to the GIT H frequency, and if the former is the case, as a rule, the Z component shows strong amplification effects, leading to the GIT peak being masked in the H/V ratio.

As aforementioned, soil-structure interactions with the observation shed could also be responsible for strong high-frequency peaks in the GIT H response function. In such a case, a collocated peak is expected in the GIT Z amplification function as well, and hence, the H/V ratio does not contain the peak observed in the GIT H response. This is the case at station TTRH02, where both GIT H and GIT Z functions indeed show a peak at the same frequency of roughly 7–8 Hz. A point to keep in mind as well is that the peak frequency of amplification is not necessarily equal to the fundamental frequency. In terms of amplitude, the H/V estimate is almost always significantly smaller than the GIT peak amplification.

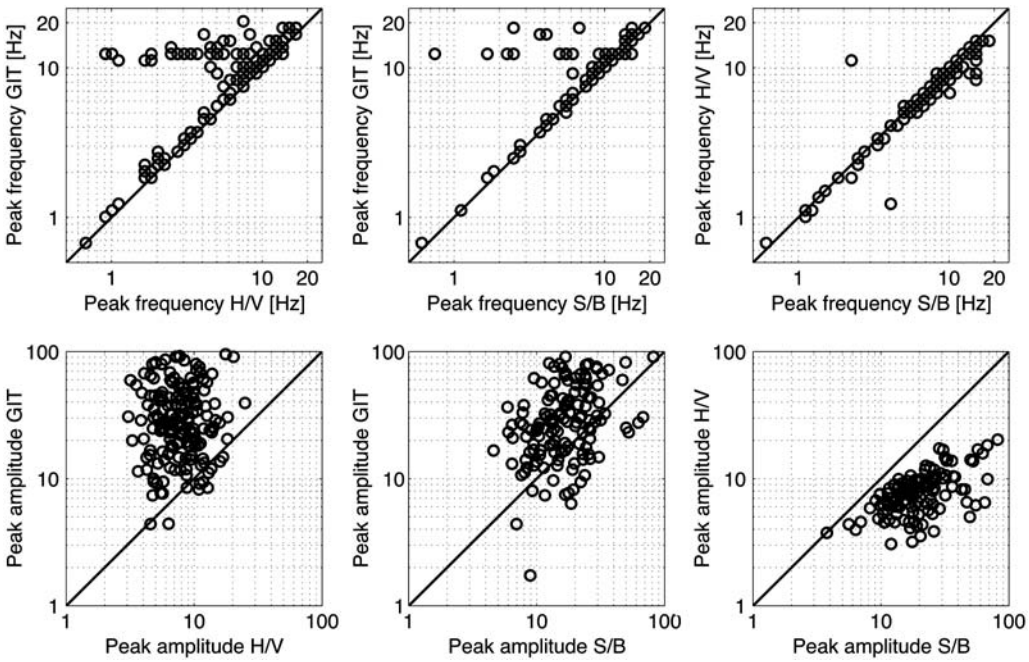

Figure 16. Peak frequency (top) and peak amplitude (bottom) comparisons between the three site response estimators GIT H, H/V, and S/B. Left: Comparison of H/V and GIT H. Middle: Comparison of S/B and GIT H. Right: Comparison of S/B and H/V.

The S/B ratios seem to do a better job in describing amplification of the H component at the surface sensor, as the results for the six stations in Figure 14 and the comparison of peak frequency and amplitude in Figure 16 indicate. This is due to the fact that even though visible in the site response contributions of the borehole stations, the amplitude of the downgoing wave effect is, in the vast majority of cases, small compared with surface amplification effects. This finding may, at first glance, look like a contradiction with respect to the surface/borehole sensor pair waveform deconvolution analysis presented in the companion paper, where downgoing waves can be clearly identified, even in some very deep boreholes. However, it is important to note that for the type of spectral analysis presented here, we smoothed the ground motion spectra around a discrete set of frequencies equidistantly spaced on a logarithmic scale. Because downgoing waves result in interference phenomena that act on narrow frequency bands (depending on the velocity structure within the borehole), the troughs induced by downgoing waves in the spectra of borehole ground motions are generally quite narrow, and typical smoothing procedures such as those used in this work are expected to lead to a reduction of these troughs. In general, the peak frequencies are very close to each other for the S/B and GIT H estimators, while the GIT peak amplification has a tendency to be somewhat larger than the S/B one. The comparison of H/V and S/B ratios shows a similar, though less pronounced, tendency when compared with H/V and GIT H. The peak frequency

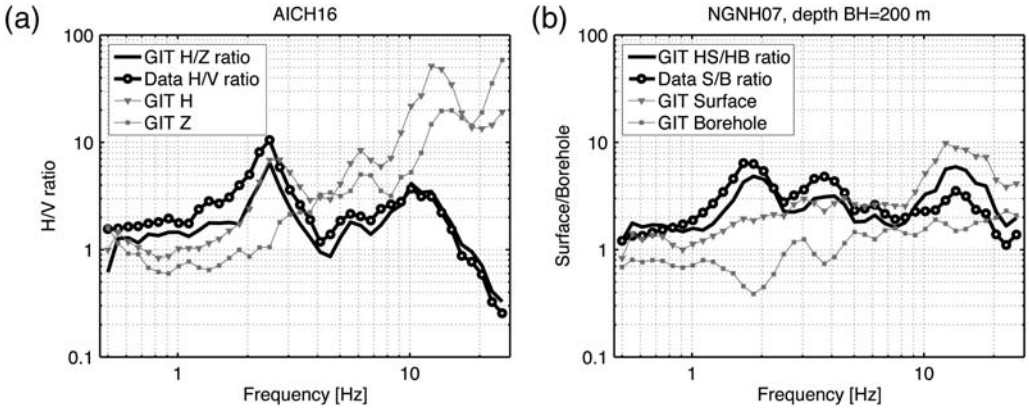

Figure 17. (a) H/V ratio compared with GIT H component results at station AICH06. Note the amplification at high frequencies on the Z component, efficiently removing the GIT peak at 12–13 Hz. (b) S/B ratio compared with GIT results at station NGNH07. Note the strong downgoing wave trough between 1 and 2 Hz, causing the largest peak in the S/B ratio.

of the H/V ratio is usually smaller than or equal to the S/B ratio peak frequency, and the peak amplitude is smaller as well.

There are a number of sites that show GIT H peak frequencies of around 12–13 Hz, but this peak frequency is significantly underestimated by the H/V one and, in fewer cases, the S/B one. Regarding the H/V ratio, this effect is due to the presence of a peak of smaller amplitude at low frequencies in the GIT H component site response in conjunction with strong amplification on the Z component at high frequencies. Note that in this case, the peak frequency is not equivalent to the fundamental frequency, and the smaller peak at low frequencies is related to the fundamental frequency. Station AICH16 (Fig. 17, left panel) provides a good example of how the H/V ratio is able to resolve the fundamental frequency of a site (around 2.5 Hz), but the peak frequency is removed due to the strong amplification of the vertical component. For a couple of sites where the S/B ratio does not reproduce the GIT H peak frequency, either significant downgoing wave troughs are causing a peak in the S/B ratio not present in the GIT H function (e.g., station NGNH07, Fig. 17, right panel: the locations of stations AICH16 and NGNH07 are depicted in fig. 5 of the companion paper) or, because the S/B ratios include the effect of high-frequency diminution in the near-surface layers, the correction of the GIT H site response functions with κ_{diff} as discussed earlier is not strong enough. Therefore, the predominant peak at 12–13 Hz of the corrected GIT H function still has a slightly larger amplitude than the fundamental frequency peak. However, because the peak at 12–13 Hz in the GIT H amplification function occurs at more than just a few stations, and its partially huge amplitude cannot be explained by simple resonance due to velocity contrasts seen in the profiles from *PS* logging alone, the question in how far soil-structure interaction effects may contribute to its generation needs to be clarified in future investigations.

Finally, there are some stations showing stronger peaks in the site response function at borehole depth as well. For instance, at stations EHMH02 and MIEH03, while the peak frequency at the surface ranges between 10–13 Hz, the borehole site response depicts a peak at higher frequencies around 18–20 Hz (Figs. 13 and 14), which coincides well with the frequency of the peak observed in the GIT amplification function of the Z component at the surface sensor (Fig. 15). From that perspective, one could speculate that this peak may be related to *S-P* converted waves as well, and Parolai *et al.* (2009) discussed the potential presence of such downgoing mode conversions in the results of downhole/surface recording pair deconvolutions. However, further analyses would need to be carried out in order to either corroborate or reject this possibility.

Discussion and Conclusions

With the results discussed in the previous sections, we have derived a full description of the ground motion FAS characteristics in Japan, from the origin of ground motions (i.e., the source spectra) to their modifications induced by effects along the travel paths (i.e., the attenuation functions) and site response at the observation sites. Using the nonparametric GIT approach, we followed the philosophy of using as many constraints as necessary yet as few as possible to solve the system of equations, especially with respect to predefining the functional forms of the different operators.

In recent years, many studies have dealt with explaining the spectral attenuation characteristics in various regions of the Japanese archipelago. Kinoshita (1994), for instance, estimated *S*-wave quality factors for the frequency range 0.5–16 Hz in the Kanto region, while Moya and Irikura (2003) derived $Q(f)$ values in the source region of the 2000 Tottori earthquake, which occurred on the southern part of the island of Honshu. The former obtained $Q(f) = 130f^{0.7}$, while the latter found $Q(f) = 43.4f^{0.67}$. Our results (which do not vary excessively from region to region) are in good agreement with these estimates, both with respect to Q_0, for which we found values ranging between about 50 and 130, and frequency dependence, for which we observe the range $N = 0.6$–0.9 (Table 2). Jin *et al.* (2000) also used a similar Q model derived from seismic coda (frequency band 1–12 Hz), $Q(f) = 75.7f^{0.81}$, to correct for seismic attenuation when deriving source parameters and site response functions along the Atotsugawa fault zone, and Choy and Boatwright (2009) estimated $Q(f) = 236f^{0.61}$ and $Q(f) = 180f^{0.6}$ from regional K-NET recordings of the 1996 Kyushu and 2000 Tottori earthquakes and frequency ranges 0.2–10 Hz and 0.2–30 Hz, respectively. We note that our Q models for crustal attenuation have been derived using only the distance range 10–50 km of the nonparametric attenuation functions, for which we can reasonably assume that the *S*-wave windows are dominantly composed of direct waves, while other authors also include regional Lg waves and use a fully parametric approach right from the beginning (Choy and Boatwright, 2009). Tsuda *et al.* (2010) found $Q(f) = 107f^{0.52}$ in the Kanto region, using a parametric GIT inversion with several subcrustal earthquakes only.

Regarding the earthquake source characteristics, we find that the source spectra generally follow the ω^2 model with self-similar scaling, and for a given seismic moment, crustal earthquakes have lower corner frequencies and hence lower stress drops (ranging around 1 MPa) than subcrustal ones (ranging around 10 MPa). We refrain from a more detailed discussion of the source parameters at this point because these are the subject of a dedicated article (Oth *et al.*, 2010) and only note that our results are in good agreement with several previous studies.

In terms of site amplification effects, we focused our study on weak and not-so-strong ground motions, using only records with PGA below $0.2g$, a focus similar to other authors (e.g., Kawase, 2006; Thompson *et al.*, 2009). Site amplification effects have been extensively studied for several subsets of the KiK-net data in recent years. Kawase (2006) compared site response functions derived from such weak motions with

those from high PGA records, identifying nonlinear effects at many stations. Assimaki *et al.* (2008) studied the S/B ratios at subsets of the KiK-net stations and came to the conclusion that, even though downgoing waves can be identified, the borehole records are not that heavily contaminated, particularly at stations where strong impedance contrasts exist, leading to the trapping of energy in the superficial layers and thus preventing the generation of downgoing waves reaching the borehole sensor. Thompson *et al.* (2009) showed that for their studied subset of KiK-net stations, the theoretical transfer function computed using propagator matrices including the downgoing wave effect depicts pronounced peaks due to the latter, which generally do not appear in the observed S/B ratios. Therefore, they conclude, similarly to Assimaki *et al.* (2008), that the borehole records are not excessively contaminated by downgoing waves and primarily relate the diminution of the downgoing wave effect to scattering effects. Our borehole GIT results are, in most cases, in agreement with the conclusions of diminution of downgoing wave effects, and because Thompson *et al.* (2009) provided an in-depth discussion on the theoretical transfer functions and their comparisons with S/B ratios, we refer the reader to their article for a thorough discussion on these issues.

Kawase (2006) showed site amplification results from weak motions for several stations on Hokkaido (figs. 12 and 13 in Kawase, 2006). A comparison of these results with our site response functions for the same stations shows little agreement. However, because Kawase (2006) used a different reference condition, a parametric inversion approach, and a different data set, a direct comparison of the results is not straightforward. Moya and Irikura (2003), on the other hand, also derived site response functions for the source region of the 2000 Tottori earthquake using an ω^2 reference source and a parametric inversion approach (see fig. 10 in their article). While at some stations (e.g., TTR007, not shown here), our site response functions show similar peaks, there is little agreement at other sites shown in their article. In particular, different from our results, their site response functions decay strongly at high frequencies, which is due to the fact that their reference source, being of the ω^2 type, keeps a constant plateau value in acceleration at high frequencies, thus shifting the high-frequency decay in the recorded ground motion spectra into the site contributions. The most recent study that we can compare our results with is the work of Tsuda *et al.* (2010). In terms of site responses (fig. 7 in their paper), our results compare very well with their findings within the frequency range 0.5–10 Hz (the range depicted in their article). We note again at this point that the source spectra and site amplification derived here were obtained without making specific model assumptions on the functional form of the attenuation operator.

Our results enable us, in conjunction with the surface/borehole sensor pair waveform deconvolution results presented in the companion paper, to systematically characterize the impact of destructive interference effects due to downgoing wave propagation on the borehole FAS, which, to our knowledge, has not yet been done using a GIT approach. We showed that the influence of downgoing waves is clearly visible in many cases; however, it is less pronounced in the GIT site response results than in the propagator time functions calculated by waveform deconvolution (see the companion paper). As discussed earlier, this reduction of downgoing wave effects in the spectral inversion is, to some extent, also linked to the smoothing of the spectra, reducing the amplitude of the destructive interference troughs in the borehole ground motion spectra. If a spectral analysis specifically targeting these effects is required, only weak smoothing of the spectra should be considered. This outcome of our study, however, also means that for typical site-response studies, the downgoing waves can be removed to a first-order approximation by appropriate spectral smoothing, and then in most cases, the S/B ratios provide a reasonable site response estimator.

Nevertheless, we confirmed with our study that downgoing waves are generally present in the borehole records and that the latter cannot be viewed as equivalent to input motion on rock conditions for engineering applications because even small downgoing wave amplitudes could have important consequences, for instance, for the calculation of GMPEs intended for use in seismic hazard computations with long return periods or site-specific hazard studies. Finally, the S/B ratios generally provide site response estimates that are more compatible with the GIT H component results than the H/V ratios, both in terms of peak frequency and amplitude, and the H/V ratios should be used with care because significant amplification effects are visible on the vertical components, most likely stemming from *S-P* phase conversions at interfaces with large impedance contrasts.

Data and Resources

The seismograms and geotechnical data used in this study were collected from the National Research Institute for Earth Science and Disaster Prevention (NIED) in Japan. The site response functions and source spectra for all stations and earthquakes used in the analysis can be obtained from the authors upon request. Waveform data can be obtained from the K-NET, KiK-net, and Hi-net websites at www.k-net.bosai.go.jp, www.kik.bosai.go.jp, and www.hinet.bosai.go.jp, respectively (last accessed April 2010).

Acknowledgments

We wish to thank the National Research Institute for Earth Science and Disaster Prevention (NIED) for making the K-NET and KiK-net data available. In the framework of this study, Domenico Di Giacomo was supported by a research grant from the European Center for Geodynamics and Seismology and was enrolled in the Ph.D. program of the University of Potsdam, Germany, during his contribution to this study. Associate Editor Zhigang Peng and the anonymous reviewers provided constructive comments that helped to improve the manuscript. This publication was supported by the National Research Fund, Luxembourg (FNR/10/AM4/26).

References

Aki, K. (1967). Scaling law of seismic spectrum, *J. Geophys. Res.* **72,** 1217–231.

Anderson, J. G., and S. E. Hough (1984). A model for the shape of the Fourier amplitude spectrum of acceleration at high frequencies, *Bull. Seismol. Soc. Am.* **74,** 1969–993.

Andrews, D. J. (1986). Objective determination of source parameters and similarity of earthquakes of different size, in *Earthquake Source Mechanics*, S. Das, J. Boatwright, and C. H. Scholz (Editors), American Geophysical Union, Washington, D.C..

Assimaki, D., W. Li, J. H. Steidl, and K. Tsuda (2008). Site amplification and attenuation via downhole array seismogram inversion: A comparative study of the 2003 Miyagi-Oki aftershock sequence, *Bull. Seismol. Soc. Am.* **98,** 301–330.

Bindi, D., R. R. Castro, G. Franceschina, L. Luzi, and F. Pacor (2004). The 1997–1998 Umbria-Marche sequence (central Italy): Source, path, and site effects estimated from strong motion data recorded in the epicentral area, *J. Geophys. Res.* **109,** B04312.

Bindi, D., S. Parolai, H. Grosser, C. Milkereit, and S. Karakisa (2006). Crustal attenuation characteristics in northwestern Turkey in the range from 1 to 10 Hz, *Bull. Seismol. Soc. Am.* **96,** 200–214.

Boore, D. M. (2003). Simulation of ground motion using the stochastic method, *Pure Appl. Geophys.* **160,** 635–676.

Boore, D. M., and W. B. Joyner (1997). Site amplifications for generic rock sites, *Bull. Seismol. Soc. Am.* **87,** 327–341.

Brune, J. N. (1970). Tectonic stress and the spectra of seismic shear waves from earthquakes, *J. Geophys. Res.* **75,** 4997–5009.

Brune, J. N. (1971). Correction. *J. Geophys. Res.* **76,** 5002.

Castro, R. R., J. G. Anderson, and S. K. Singh (1990). Site response, attenuation and source spectra of *S* waves along the Guerrero, Mexico, subduction zone, *Bull. Seismol. Soc. Am.* **80,** 1481–1503.

Castro, R. R., F. Pacor, A. Sala, and C. Petrungaro (1996). *S* wave attenuation and site effects in the region of Friuli, Italy, *J. Geophys. Res.* **101,** 22355–22369.

Choy, G. L., and J. Boatwright (2009). Differential energy radiation from two earthquakes in Japan with identical M_w: The Kyushu 1996 and Tottori 2000 earthquakes, *Bull. Seismol. Soc. Am.* **99,** 1815–1826.

Drouet, S., S. Chevrot, F. Cotton, and A. Souriau (2008). Simultaneous inversion of source spectra, attenuation parameters, and site responses: Application to the data of the French Accelerometric Network, *Bull. Seismol. Soc. Am.* **98,** 198–219.

Hanks, T. C. (1982). f_{max}, *Bull. Seismol. Soc. Am.* **72,** 1867–1879.

Hartzell, S., A. Leeds, A. Frankel, and J. Michael (1996). Site response for urban Los Angeles using aftershocks of the Northridge earthquake, *Bull. Seismol. Soc. Am.* **86,** S168–S192.

International Code Council (2006). *International Building Code (IBC)*, International Code Council, Falls Church, Virginia.

Jin, A., C. A. Moya, and M. Ando (2000). Simultaneous determination of site responses and source parameters of small earthquakes along the Atotsugawa fault zone, central Japan, *Bull. Seismol. Soc. Am.* **90,** 1430–1445.

Kawase, H. (2006). Site effects derived from spectral inversion method for K-NET, KiK-net, and JMA strong-motion network with special reference to soil nonlinearity in high PGA records, *Bull. Earthq. Res. Inst. Univ. Tokyo* **81,** 309–315.

Kinoshita, S. (1994). Frequency-dependent attenuation of shear waves in the crust of the southern Kanto area, Japan, *Bull. Seismol. Soc. Am.* **84,** 1387–1396.

Kinoshita, S., and M. Ohike (2002). Scaling relations of earthquakes that occurred in the upper part of the Philippine Sea plate beneath the Kanto region, Japan, estimated by means of borehole recordings, *Bull. Seismol. Soc. Am.* **92,** 611–624.

Konno, K., and T. Ohmachi (1998). Ground-motion characteristics estimated from spectral ratio between horizontal and vertical components of microtremor, *Bull. Seismol. Soc. Am.* **88,** 228–241.

Morozov, I. B. (2008). Geometrical attenuation, frequency dependence of *Q*, and the absorption band problem, *Geophys. J. Int.* **175,** 239–252.

Maeda, T. (2004). Observatory shed effect on strong motion records identified by micro-tremor measurement, in *Proc. of the Thirteenth World Conf. on Earthq. Eng.*, Paper No. 568.

Moya, A., and K. Irikura (2003). Estimation of site effects and *Q* factor using a reference event, *Bull. Seismol. Soc. Am.* **93,** 1730–1745.

Okada, Y., K. Kasahara, S. Hori, K. Obara, S. Sekiguchi, H. Fujiwara, and A. Yamamoto (2004). Recent progress of seismic observation networks in Japan-Hi-net, F-net, K-NET and KiK-net, *Earth Planets Space* **56,** xv–xxviii.

Oth, A., D. Bindi, S. Parolai, and F. Wenzel (2008). *S*-wave attenuation characteristics beneath the Vrancea region in Romania: New insights from the inversion of ground-motion spectra, *Bull. Seismol. Soc. Am.* **98,** 2482–2497.

Oth, A., S. Parolai, D. Bindi, and F. Wenzel (2009). Source spectra and site response from *S* waves of intermediate-depth Vrancea, Romania, earthquakes, *Bull. Seismol. Soc. Am.* **99,** 235–254.

Oth, A., S. Parolai, and D. Bindi (2011). Spectral analysis of K-NET and KiK-net data in Japan, Part I: Database compilation and peculiarities, *Bull. Seismol. Soc. Am.* **101,** 652–666.

Oth, A., D. Bindi, S. Parolai, and D. Di Giacomo (2010). Earthquake scaling characteristics and the scale-(in)dependence of seismic energy-to-moment ratio: Insights from KiK-net data in Japan, *Geophys. Res. Lett.* **37,** L19304, doi 10.1029/2010GL044572.

Paige, C. C., and M. A. Saunders (1982). LSQR: An algorithm for sparse linear equations and sparse least squares, *ACM Trans. Math. Software* **8,** 43–71.

Papageorgiou, A. S., and K. Aki (1983). A specific barrier model for the quantitative description of inhomogeneous faulting and the prediction of strong ground motion. Part I: Description of the model, *Bull. Seismol. Soc. Am.* **73,** 693–722.

Parolai, S., and D. Bindi (2004). Influence of soil-layer properties on *k* evaluation, *Bull. Seismol. Soc. Am.* **94,** 349–356.

Parolai, S., and S. M. Richwalski (2004). The importance of converted waves in comparing H/V and RSM site response estimates, *Bull. Seismol. Soc. Am.* **94,** 304–313.

Parolai, S., A. Ansal, A. Kurtulus, A. Strollo, R. Wang, and J. Zschau (2009). The Ataköy vertical array (Turkey): Insights into seismic wave propagation in the shallow-most crustal layers by waveform deconvolution, *Geophys. J. Int.* **178,** 1649–1662.

Parolai, S., D. Bindi, and P. Augliera (2000). Application of the generalized inversion technique (GIT) to a microzonation study: Numerical simulations and comparison with different site-estimation techniques, *Bull. Seismol. Soc. Am.* **90,** 286–297.

Parolai, S., D. Bindi, M. Baumbach, H. Grosser, C. Milkereit, S. Karakisa, and S. Zunbul (2004). Comparison of different site response estimation techniques using aftershocks of the 1999 Izmit earthquake, *Bull. Seismol. Soc. Am.* **94,** 1096.

Pei, S., Z. Cui, Y. Sun, M. N. Toksoz, C. A. Rowe, X. Gao, J. Zhao, H. Liu, J. He, and F. D. Morgan (2009). Structure of the upper crust in Japan from *S*-wave attenuation tomography, *Bull. Seismol. Soc. Am.* **99,** 428–434.

Salazar, W., V. Sardina, and J. de Cortina (2007). A hybrid inversion technique for the evaluation of source, path, and site effects employing *S*-wave spectra for subduction and upper-crustal earthquakes in El Salvador, *Bull. Seismol. Soc. Am.* **97,** 208–221.

Takenaka, H., Y. Mamada, and H. Futamure (2003). Near-source effect on radiation pattern of high-frequency *S* waves: Strong SH-SV mixing observed from aftershocks of the 1997 northwestern Kagoshima, Japan, earthquakes, *Phys. Earth Planet. In.* **137,** 31–43.

Thompson, E. M., L. G. Baise, R. E. Kayen, and B. B. Guzina (2009). Impediments to predicting site response: Seismic property estimation and modeling simplifications, *Bull. Seismol. Soc. Am.* **99,** 2927–2949.

Tsuda, K., R. J. Archuleta, and K. Koketsu (2006). Quantifying the spatial distribution of site response by use of the Yokohama high-density strong-motion network, *Bull. Seismol. Soc. Am.* **96,** 926–942.

Tsuda, K., K. Kokestsu, Y. Hisada, and T. Hayakawa (2010). Inversion analysis of site responses in the Kanto basin using data from a dense strong motion seismograph array, *Bull. Seismol. Soc. Am.* **100,** 1276–1287.

Yoshimura, C., H. Hibino, Y. Uchiyama, T. Maeda, N. Kurauchi, and S. Aoi (2003). Vibration characteristics of the observation house at KiK-net Hino, *2003 Japan Earth and Planetary Science Joint Meeting* (in Japanese with English abstract).

European Center for Geodynamics and Seismology
19, rue Josy Welter
L-7256 Walferdange, Grand-Duchy of Luxembourg
adrien.oth@ecgs.lu
(A.O.)

Center for Disaster Management and Risk Reduction Technology (CEDIM)
Helmholtz Center Potsdam
GFZ German Research Center for Geosciences
Telegrafenberg, 14473
Potsdam, Germany
bindi@gfz-potsdam.de
(D.B.)

Earthquake Risk and Early Warning Section
Helmholtz Center Potsdam
GFZ German Research Center for Geosciences
Telegrafenberg, 14473
Potsdam, Germany
parolai@gfz-potsdam.de
domenico@isc.ac.uk
(S.P., D.D.)

Manuscript received 19 May 2010